Non-intrusive Characterisation of Particle Cluster Behaviours in a Riser through Electrostatic and Vibration Sensing

Jingyuan Sun[a,b], Yong Yan[b,*]

[a] State Key Laboratory of Chemical Engineering, College of Chemical and Biological Engineering, Zhejiang University, Hangzhou 310027, P. R. China

[b] School of Engineering and Digital Arts, University of Kent, Canterbury, Kent CT2 7NT, U.K.

Abstract

Particle clusters are important mesoscale flow structures in gas-solid circulating fluidised beds (CFBs). An electrostatic sensing system and two accelerometers are installed on the riser of a CFB test rig to collect signals simultaneously. Cross correlation, Hilbert-Huang transform (HHT), V-statistic analysis, and wavelet transform are applied for signal identification and cluster characterisation near the wall. Solids velocities are obtained through cross correlation. Non-stationary and non-linear characteristics are distinctly exhibited in the Hilbert spectra of the electrostatic and vibration signals, and the cluster dynamic behaviours are represented by the energy distributions of the signal intrinsic mode functions (IMFs). The cycle feature and main cycle frequency of cluster motion are characterised through V-statistic analysis of the vibration signals. Consistent characteristic information about particle clusters is extracted from the electrostatic and vibration signals. Furthermore, a cluster

* Corresponding author. E-mail addresses: y.yan@kent.ac.uk

identification criterion for electrostatic signals is proposed, including a fixed and a wavelet dynamic thresholds, based on which the cluster time fraction, average cluster duration time, cluster frequency, and average cluster vertical size are quantified. Especially, the cluster frequency obtained from this criterion agrees well with that from the aforementioned V-statistic analysis. Results from this work provide a new non-intrusive approach to the characterisation of cluster dynamic behaviours and their effects on the flow field.

Keywords: Riser; Electrostatic sensing; Vibration sensing; Fluctuation signal processing; Cluster characteristic parameter

1. Introduction

Gas-solid circulating fluidisation is an important unit operation with extensive applications in industrial processes, such as fluid catalytic cracking, chemical looping, coal and biomass gasification, to name but a few. Gas-solid flow inside the riser of a CFB is inherently dynamic and chaotic, leading to the formation of transient mesoscale flow structures manifesting as particle clusters [1,2], referred to as particle groups with high height-to-width ratios, higher solids contents than the surrounding, and significant existence in the time scale [3]. Particle clusters are mainly distributed near the wall, affecting significantly the flow hydrodynamics and riser performance [1], and if evolving to particle agglomerates, severe fluidisation faults (e.g., hot spots, explosive polymerisation, reactor shutdown) are likely to be caused [4]. Therefore, it is essential to characterise particle cluster behaviours and their effects on the flow field,

especially near the wall.

Extensive experimental work has been conducted in attempts to acquire the cluster-related parameters. For instance, capacitance and optical fibre probes have been used to sense solids holdup fluctuations in risers, based on which the cluster sizes and distributions [5-8], cluster counts [7], and cluster appearance probabilities, durations, and frequencies [1,2,9-11] have been characterised. However, these probes are intrusive and hence suffer from a disadvantage of interferences to the flow fields. The imaging technique provides a non-intrusive approach to cluster characterisation. Horio and Kuroki [12] observed the paraboloid average shape of a cluster and determined the cluster sizes and velocity distributions through image processing. Mondal et al. [3,13] evaluated the cluster length scales and the solids holdup inside clusters with the aid of video record and image analysis. Despite a full-field flow visualisation provided, the imaging technique always requires uniform illuminations and otherwise the presence of shadows will affect the measurement reliability. In addition, the imaging technique is applicable to pseudo-two-dimensional and the dilute regions of three-dimensional risers, whereas the measurement reliability is significantly influenced when being applied to denser three-dimensional risers. Another visualisation technique is named the thermal image velocimetry [14], developed to measure the cluster velocity and cluster contact time with the wall. However, this technique requires an extra heating section and a special wall allowing the radiant signal transmission, leading to less portability and flexibility.

Non-intrusive electrostatic induction sensors are increasingly applied to probing

the hydrodynamic characteristics of gas-solid fluidisation systems via sensing the electrostatic fluctuations caused by the particle-particle and particle-wall interactions [15-18]. Because of the high sensitivity of the electrostatic signals to the moving particles, rich information regarding the solids flow field and flow structures is embedded in the electrostatic signals [19]. Therefore, the electrostatic induction sensors are naturally applicable to the non-intrusive characterisation of particle cluster behaviours through appropriate signal processing. To date some researchers have made efforts in the measurement of solids velocities and charge levels in fluidised beds by using electrostatic induction sensors [15-18]. However, very limited relevant work has been conducted on particle cluster characterisation. Sun and Yan [19] extracted the coherent structure dynamic information in a riser through electrostatic signal analysis, yet focusing on the influence of coherent structures on the flow intermittency. In addition, accelerometers are desirable non-intrusive tools that enable the measurement of flow-induced vibrations experienced by fluidised beds and hence the characterisation of flow structure behaviours [4]. Accelerometers have been used for monitoring the bed fluidity [20], detecting the agglomerate occurrence [20], and characterising the particle motion [21] and the bulk and bubble dynamics [22-25]. As bubbles and particle clusters are both classified as mesoscale flow structures [22,26], accelerometers should also be applicable to cluster behaviour characterisation. However, to the best of our knowledge no relevant work has been carried out until now.

In terms of the cluster identification through signal analysis, an appropriate threshold plays an important role. Single-value thresholds (e.g. times of the standard

deviations above the mean voltages) have been applied to solids holdup signals from capacitance and optical fibre probes [9,27,28]. Considering that such thresholds may lead to dynamic information loss, wavelet transform was then used for the threshold determination of optical fibre signals, because of its capability of demarcating different flow scales (microscale, mesoscale, macroscale) [1,2,29]. Although an electrostatic sensor cannot directly provide solids holdup data, it is still possible to identify clusters from the electrostatic signals through an appropriate threshold separation, because of the strong dependence of the electrostatic signals on the solids holdup.

In this study, an electrostatic induction sensing system and two high-sensitivity accelerometers are installed on the riser of a gas-solid CFB test rig to collect the electrostatic and vibration signals simultaneously. As these signals are generated by non-linear, non-stationary, and multiscale flow behaviours, a localised and adaptive analysis method, HHT, is used for signal processing, aimed at characterising particle cluster behaviours and their hydrodynamic effects near the wall. V-statistic analysis is employed to quantify the cyclic features of particle cluster motion. Furthermore, wavelet transform is applied to cluster signal extraction from the electrostatic signals. A cluster identification criterion is proposed, including a fixed and a wavelet dynamic thresholds, based on which the cluster characteristic parameters are quantified. Localised solids velocities are also obtained via cross correlation of the electrostatic signals.

2. Experimental setup

Figure 1 shows the layout of a Perspex-made gas-solid CFB test rig, mainly

composed of a riser, a downer, a cyclone separator, and a butterfly valve. The riser is of a cylinder with an inner diameter of 0.1 m and a height of 2.1 m. Amino plastic particles (Martyn's Bargains Ltd, U.K.) with an average diameter of 0.505 mm and density of 1500 kg/m^3 are employed as the fluidisation material. Air supplied by a compressor passes through a pressure regulator, a diaphragm valve, a flowmeter, and then enters the bottom of the riser. The variation ranges of the superficial gas velocity (U_g) and solids flux (G_s) are 3.9 m/s ~ 5.0 m/s and 4.0 kg/(m^2·s) ~ 35.0 kg/(m^2·s), respectively. The height of the initial static bed in the downer was about 1.0 m. Experiments were carried out at an ambient temperature of 21 ℃ in an air conditioned laboratory.

The electrostatic sensing system shown in Figure 1 consists of four electrostatic sensor arrays, labelled as 1, 2, 3, and 4, respectively, fitted flush with the inner riser wall. Figure 2 shows the top view of these sensor arrays. Each sensor array includes three parallel identical arc-shaped electrodes, which have an axial height of 5 mm and a central angle of 70°. The centre-to-centre distance between two adjacent electrodes in each array is 20 mm. A weak signal induced in an electrode is first converted into a voltage signal and then pre-amplified before being further amplified through a signal conditioning circuit. High-frequency noises are removed through a low-pass filter with a cut-off frequency of 2 kHz. To collect the vibration signals generated by the particle impacts on the wall, two high-sensitivity accelerometers (Brüel & Kjær 4508-B-002) are mounted on the outer wall of the riser through two mounting slots with glue, as close as possible to the lower and upper electrostatic sensor arrays (1 and 3), respectively. The accelerometers have a sensitivity of 1000 mV/g and a resonance

frequency of 25 kHz. Both the electrostatic sensors and accelerometers are connected to a DAQ device (NI USB-6353). Before any signal acquisition, particles in the CFB were fluidised at a certain superficial gas velocity for at least 20 min to ensure that a saturated charged state was achieved. This pre fluidisation time was based on the preliminary analysis of electrostatic signal variations and also adopted in our previous work for the same experimental system [19]. Electrostatic and vibration signals were then sampled simultaneously at a frequency of 16 kHz with a duration of 200 s.

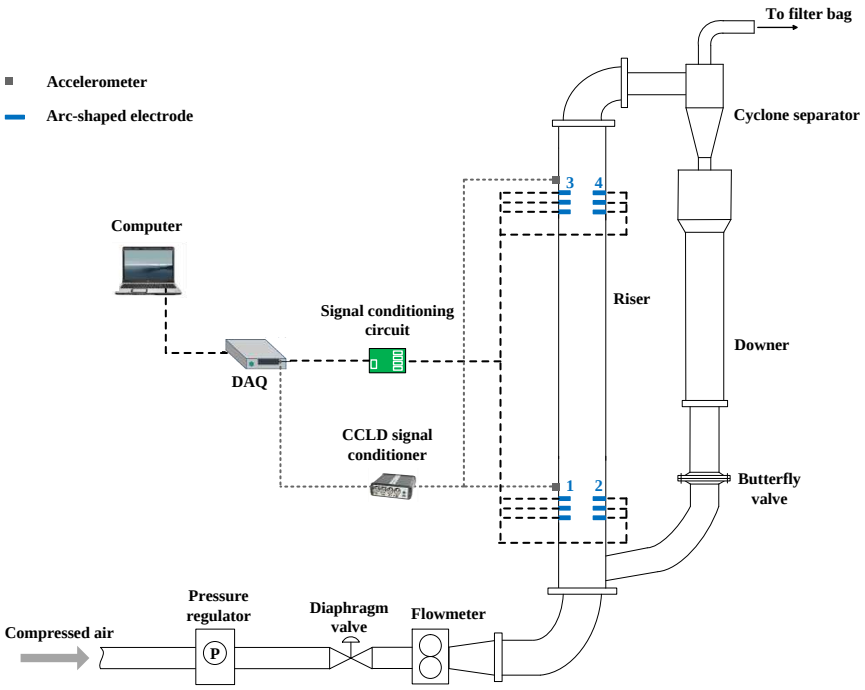

Figure 1. Layout of the gas-solid CFB test rig

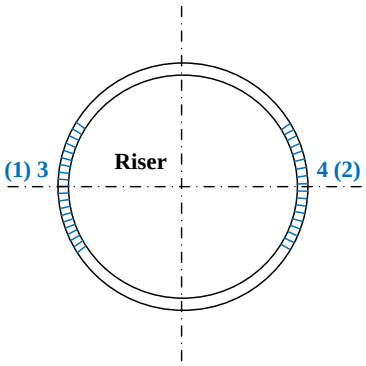

Figure 2. Top view of the electrostatic sensor arrays

3. Analysis methods

3.1. Solids velocity measurement

The applicability of arc-shaped electrostatic sensors to the solids velocity measurement in a riser has been demonstrated in our previous work [19] and is only introduced briefly here for the convenience of the reader. When particles pass through a pair of electrodes in a sensor array, two similar signals are induced in the upstream (lower) and downstream (upper) electrodes. The correlation solids velocity is calculated from,

$$v_c = \frac{L}{\tau} \tag{1}$$

where L is the centre-to-centre distance between the upstream and downstream electrodes, τ the time delay between the two signals. The normalised cross-correlation function between the two signals x_i and y_i (i=1, 2, …, N) is expressed as,

$$R_{xy}(m) = \frac{\sum_{i=1}^{N}\left(x_i - \bar{x}\right)\left(y_{i+m} - \bar{y}\right)}{\sqrt{\sum_{i=1}^{N}\left(x_i - \bar{x}\right)^2}\sqrt{\sum_{i=1}^{N}\left(y_i - \bar{y}\right)^2}} \tag{2}$$

where N is the number of samples in the correlation computation, m (m=0, 1, 2, …, N)

the number of delayed points, $\overline{x}$ and $\overline{y}$ the mean values of the two signals, respectively. The location of the dominant peak in the correlation function indicates the time delay τ, and the dominant peak is regarded as the correlation coefficient. In this study, the correlation computation for each pair of electrodes took 16384 (2^{14}) samples from both the upstream and downstream signals during each data processing cycle. A total of 195 solids velocity and correlation coefficient readings were taken over a period of 200 s under each operation condition.

3.2. Hilbert-Huang transform

Compared to the commonly used Fourier spectral analysis, HHT is more suitable for the multi-resolution analysis of non-linear and non-stationary signals, which are typically generated in a riser [30,31]. HHT has been applied successfully to the pressure fluctuation analysis in two- and three-phase fluidised beds [32,33] and electrostatic signal analysis in a dense-phase pneumatic conveying pipe [34]. It consists of two steps [34,35]. First, a time series signal, x(t), is decomposed into a finite set of intrinsic mode functions (IMFs), $c_i(t)$ (i=1, 2, …, n associated with various time scales), and the residual, $r_n(t)$, through an empirical mode decomposition (EMD) process. The original signal can thus be reconstructed through the superposition of the IMFs and the residual,

$$x(t) = \sum_{i=1}^{n} c_i(t) + r_n(t) \tag{3}$$

where n is the number of the IMFs, depending on the operation conditions, and t is the time. Second, Hilbert transform is applied to each IMF to obtain a complex representation of the IMF, $y_i(t)$,

$$y_i(t) = \frac{1}{\pi} P \int_{-\infty}^{\infty} \frac{c_i(\tau)}{t-\tau} d\tau \tag{4}$$

where P is the Cauchy principal value. An analytical signal, $z_i(t)$, is thus defined from $c_i(t)$ and $y_i(t)$ as,

$$z_i(t) = c_i(t) + jy_i(t) = a_i(t) e^{j\theta_i(t)} \tag{5}$$

where $a_i(t)$ is the amplitude, $\theta_i(t)$ the phase angle. $a_i(t)$ and $\theta_i(t)$ are defined as,

$$a_i(t) = \sqrt{(c_i(t))^2 + (y_i(t))^2} \tag{6}$$

$$\theta_i(t) = \arctan\left(\frac{y_i(t)}{c_i(t)}\right) \tag{7}$$

Last, the instantaneous frequency of each IMF, $f_i(t)$, is calculated from,

$$f_i(t) = \frac{1}{2\pi} \frac{d\theta_i(t)}{dt} \tag{8}$$

The original signal is then expressed as,

$$x(t) = Re\left(\sum_{i=1}^{n} a_i(t) e^{j2\pi \int f_i(t) dt}\right) \tag{9}$$

It is thus possible to represent both the amplitude and instantaneous frequency as time functions, and the frequency-time distribution of the squared amplitudes is known as the Hilbert spectrum. In addition, the energy of each IMF, E_i, is calculated from [31],

$$E_i = \int_0^{\infty} |c_i(t)|^2 dt \tag{10}$$

The total energy of the original signal, E, equals the sum of the energy of the IMFs when the residual, $r_n(t)$, is ignored,

$$E = \sum_{i=1}^{n} E_i \tag{11}$$

The energy fraction of each IMF, p_i, is calculated from,

$$p_i = \frac{E_i}{E} \tag{12}$$

3.3. Rescaled range analysis and V statistic

Rescaled range (R/S) analysis was first introduced by Hurst [36] for describing the long-term memory of a time series, and has been applied successfully to multiphase flow systems [37-40]. The detailed algorithm of R/S analysis has been presented in the reference [41]. In short, a time series signal, x(t), is divided into time intervals with a length of n. The range function, R(t, n), and the standard deviation, S(t, n), follow an empirical power law expressed as,

$$\frac{R(t,n)}{S(t,n)} \propto n^{H} \tag{13}$$

where H is the Hurst exponent varying between 0 and 1. H higher than 0.5 indicates a persistent series, in which an increase in the values over a certain time interval will be most likely followed by an increase over that interval, and vice-versa. H lower than 0.5 and equalling to 0.5 indicate an anti-persistent series and a stochastic (uncorrelated) series, respectively. In addition, if a cyclic behaviour is exhibited in the signal, H changes at certain values of n and the plot of $\lg\left(\frac{R(t,n)}{S(t,n)}\right)$ vs. $\lg(n)$ is no longer a straight line. The break in this plot corresponds to the cycle time [42]. However, it is usually difficult to determine the exact location of the break in the $\lg\left(\frac{R(t,n)}{S(t,n)}\right)$ vs. $\lg(n)$ plot. The V statistic is thus defined as [43]

$$V_n = \frac{R(t,n)}{S(t,n)\sqrt{n}} \tag{14}$$

When the break is between two segments with the slopes, H, higher and lower than 0.5, respectively, the V statistic transforms the break into a more easily identified peak in

the V_n vs. $\lg(n)$ plot [43,44].

3.4. Wavelet transform and cluster characteristic parameters

Wavelet transform, in combination with a time-independent threshold criterion, is used for cluster identification from the electrostatic signals. Wavelet transform allows the extraction of different frequency ranges of a signal through a repeated signal decomposition into lower-frequency approximations and higher-frequency details [45]. The transform on a discrete signal is carried out by discrete wavelet transform (DWT). The essence of DWT is to expand a signal, x(t) (t=1, 2, …, N), as a sum of base functions, $\phi_{j,k}(t)$ and $\psi_{j,k}(t)$, produced by the dilations and translations of an orthogonal father wavelet function, ϕ, and a mother wavelet function, ψ [29],

$$\phi_{j,k}(t) = 2^{-j/2}\phi\left(\frac{t-2^j k}{2^j}\right) \quad j,k \in I \tag{15}$$

$$\psi_{j,k}(t) = 2^{-j/2}\psi\left(\frac{t-2^j k}{2^j}\right) \quad j,k \in I \tag{16}$$

where $k=1, 2, \ldots, N/2^j$ is the time shift and j=1, 2, …, J is the decomposition level. The wavelet transform of x(t) is given as

$$a_{J,k} = \int x(t)\phi_{J,k}(t)\,dt \tag{17}$$

$$d_{j,k} = \int x(t)\psi_{j,k}(t)\,dt \tag{18}$$

where $a_{J,k}$ and $d_{j,k}$ are the lower-frequency approximation and higher-frequency detail wavelet coefficients, respectively. x(t) can be decomposed into orthogonal components at different resolutions, represented by the approximation subsignal, $A_J(t)$, and detail subsignal, $D_j(t)$ [45],

$$A_J(t) = \sum_k a_{J,k}\phi_{J,k}(t) \quad J,k \in I \tag{19}$$

$$D_j(t) = \sum_k d_{j,k}\psi_{j,k}(t) \quad j,k \in I \tag{20}$$

where $D_j(t)$ corresponds to a frequency range of $[f_s/2^{j+1}, f_s/2^j]$ and $A_J(t)$ to $[0, f_s/2^{J+1}]$. Here f_s is the sampling frequency and 2^j is the scale factor at the level j. In this study, because of the good localisation and extremely small error of signal reconstruction [29], Daubechies3 is used for wavelet transform and dynamic threshold determination of the electrostatic signals, based on which the cluster characteristic parameters are determined. The definitions of these parameters are given as follows [10,28],

1) Cluster time fraction F_{cl}: the fraction of the total time when particle clusters exist within the electrode sensing zone, calculated by the ratio of the total cluster duration time to the total sampling time T,

$$F_{cl} = \frac{\sum_{i=1}^{n_{cl}} \tau_i}{T} \tag{21}$$

$$\tau_i = t_{ia} - t_{ib} \tag{22}$$

where τ_i is the duration time of the i^{th} particle cluster, t_{ia} and t_{ib} the start and end times of the existence of the i^{th} particle cluster.

2) Average cluster duration time τ_{cl}: the average duration time of particle clusters existing within the electrode sensing zone, calculated by the total cluster duration time divided by the total number of clusters n_{cl} within the sampling time T. n_{cl} is represented by the number of peaks above the corresponding threshold values,

$$\tau_{cl} = \frac{\sum_{i=1}^{n_{cl}} \tau_i}{n_{cl}} \tag{23}$$

3) Cluster frequency f_{cl}: the occurrence frequency of particle clusters within the electrode sensing zone, calculated from n_{cl} and T,

$$f_{cl} = \frac{n_{cl}}{T} \tag{24}$$

4) Average cluster vertical size L_{cl}: the characteristic dimension of a particle cluster, estimated from the local average solids velocity and average cluster duration time,

$$L_{cl} = u_s \tau_{cl} \tag{25}$$

Parameters defined in Eqs. (21)~(25) enable a quantitative and detailed description of the cluster dynamic behaviours in the riser.

4. Results and discussion

4.1. Solids velocity

As the arc-shaped electrodes are mounted flush with the wall of the riser, solids velocities obtained from the electrostatic signals mainly reflect the solids motion in the near-wall sensitive zones of the electrodes. Figure 3 shows typical variations of solids velocity with the time obtained from the 'left' sensor array 3. The result at h=1860 mm is from the correlation between the two signals at h=1850 mm and h=1870 mm, respectively, while that at h=1880 mm is from the two signals at h=1870 mm and h=1890 mm, respectively. The two curves exhibit high similarity, indicating that within the axial distance of a sensor array, the solids velocity only changes slightly and the correlation computation is hence verified. In addition, the solids velocities fluctuate significantly around the average values, indicating that particles in the riser move upward and downward very quickly due to the strong influences of chaotic gas flow, particle-particle interactions and wall effects. The direction and magnitude of the average solids velocity are comprehensive results of the local particles motion.

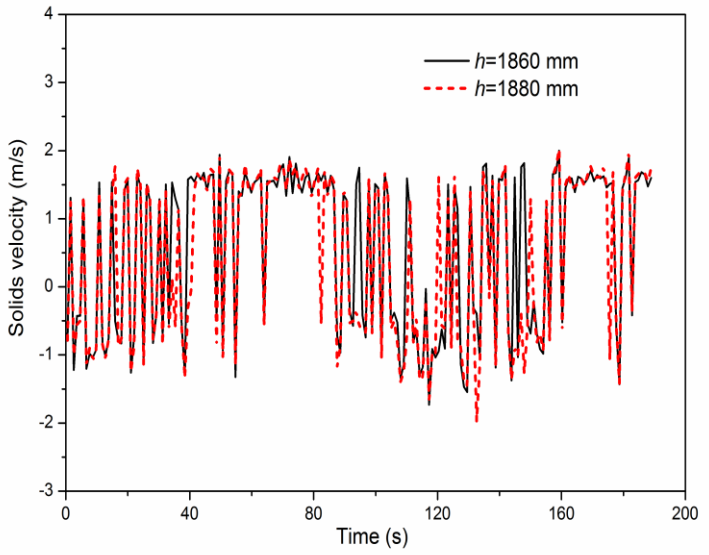

Figure 3. Variations of solids velocity with the time from the left sensor array 3, U_g=5.0 m/s, G_s=20.0 kg/(m^2·s)

Figure 4 shows the axial distributions of the time-averaged solids velocity under different operation conditions. Results from the left sensor arrays 1 and 3 are adopted for analysis. At U_g=3.9 m/s and G_s=4.0 kg/(m^2·s) the flow pattern in the riser is pneumatic conveying, in which the axial distribution of solids holdup is relatively uniform. Particles are accelerated upward rapidly at the bottom due to the velocity difference between the gas and solids phases. The solids upward velocity then decreases with the height due to the energy consumption for transporting particles against gravity, as shown in Figure 4(a). When G_s is increased to 8.0 kg/(m^2·s), the solids holdup (especially near the wall) increases and the tendency of cluster formation is enhanced, leading to the decrease of solids upward velocities near the wall, even to negative values [46]. Since further increasing G_s results in unstable fluidisation status, only two G_s are adopted at U_g=3.9 m/s, as shown in Figure 4(a) and similarly hereinafter. At a higher

U_g, the solids upward velocities near the wall also decrease significantly with the solids flux to negative values, as shown in Figures 4(b) and (c). According to the experimental observation, core-annulus flow patterns are formed at G_s=20.0 kg/(m^2·s) and G_s=35.0 kg/(m^2·s). Particle clusters are generated and continuously fall along the wall, thus contributing to the negative solids velocity values. In addition, the axial distribution of solids holdup becomes non-uniform under these conditions. The higher solids holdup at the bottom intensifies the formation of falling clusters, while in the diluter top region the cluster formation is relatively weakened. Therefore, the solids downward velocity decreases with the height at G_s=20.0 kg/(m^2·s) and G_s=35.0 kg/(m^2·s). Particularly at U_g=4.6 m/s, the solids velocities at G_s=20.0 kg/(m^2·s) and G_s=35.0 kg/(m^2·s) are close to each other. This is because a significant number of particle clusters exist under both the two conditions and are distributed in the whole riser, resulting in less variations of solids velocity with G_s, as shown in Figure 4(b). Figure 4 also shows that the solids downward velocity decreases and the upward velocity increases with the superficial gas velocity due to the increased drag force between the gas and solids phases.

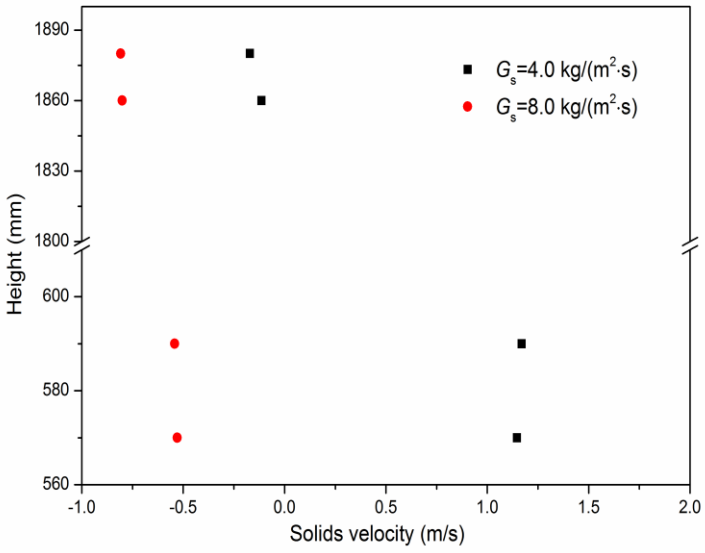

(a) U_g=3.9 m/s

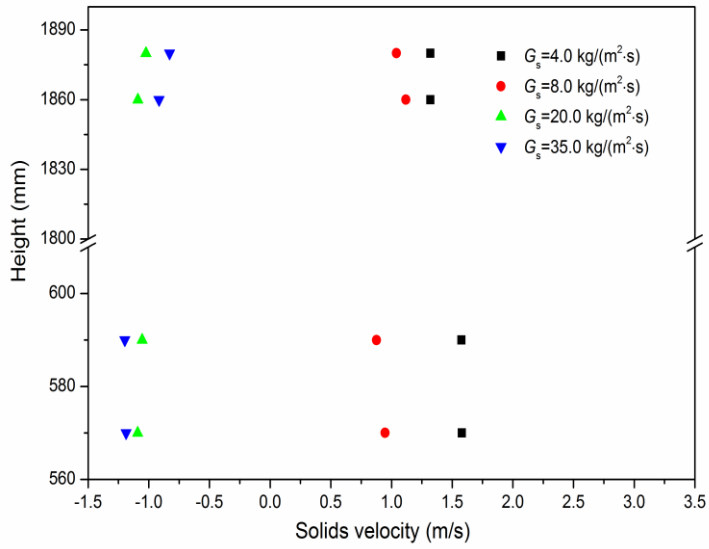

(b) U_g=4.6 m/s

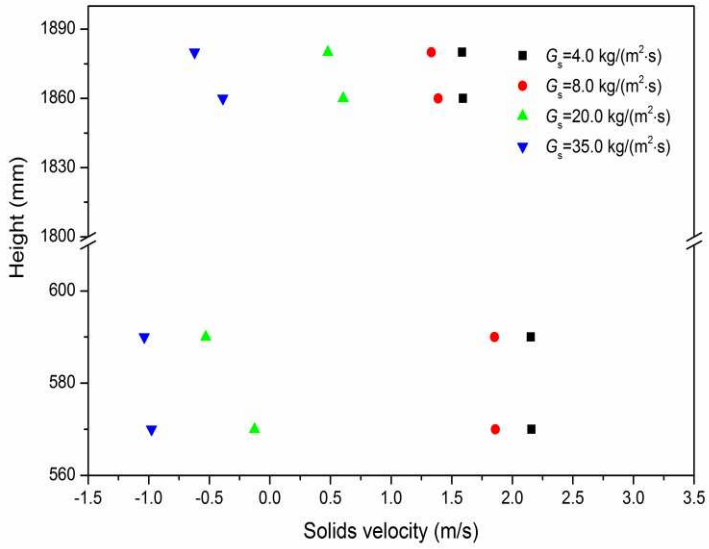

(c) U_g=5.0 m/s

Figure 4. Axial distributions of the time-averaged solids velocity from the left sensor arrays 1 and 3 under different operation conditions

Table 1 lists the time-averaged correlation coefficients from the left sensor arrays 1 and 3s. Correlation coefficients at all the heights increase basically with the solids

flux and decrease with the superficial gas velocity, indicating an enhanced similarity between the upstream and downstream electrostatic signals at a higher solids holdup, and vice versa. This is due to the shortened mean free path of particles when the solids holdup is increased and particle clusters appear, leading to less changes of solids motion characteristics within the distance between two adjacent electrodes. Moreover, the correlation coefficients for Runs 5 and 6 are higher than the rest because of the more significant core-annulus flow and stronger cluster motion under these conditions. No significant variations in correlation coefficients with the height are evident, due to the complex comprehensive effects of solids velocity and holdup on the signal similarity at different heights.

Table 1 Time-averaged correlation coefficients from the left sensor arrays 1 and 3 under different operation conditions

Run	U_g (m/s)	G_s (kg/(m^2·s))	Correlation coefficient			
			h=570 mm	h=590 mm	h=1860 mm	h=1880 mm
1	3.9	4.0	0.49	0.50	0.61	0.59
2	3.9	8.0	0.67	0.69	0.77	0.77
3	4.6	4.0	0.61	0.61	0.59	0.60
4	4.6	8.0	0.67	0.65	0.48	0.49
5	4.6	20.0	0.76	0.82	0.81	0.80
6	4.6	35.0	0.71	0.79	0.78	0.78
7	5.0	4.0	0.62	0.66	0.59	0.62
8	5.0	8.0	0.52	0.55	0.48	0.45

9	5.0	20.0	0.66	0.68	0.65	0.66
10	5.0	35.0	0.68	0.76	0.71	0.73

4.2. Hilbert-Huang transform and fluctuation energy distribution

4.2.1. Electrostatic signal analysis

According to the preliminary power spectral analysis, the frequency components of electrostatic signals are distributed in 0~200 Hz. Therefore, the electrostatic signals sampled are firstly resampled to 400 Hz and then decomposed into IMFs with different scales and multiresolution levels. Figure 5 shows the Hilbert spectra of electrostatic signals from the left sensor array 3 at h=1870 mm, describing the local characteristics and time-frequency-energy distribution of the fluctuation signals. The Y axis represents the time-dependent instantaneous frequencies of the IMFs and each colour bar on the right side, ranging from dark blue to dark red, indicates the fluctuation amplitude (energy) varying from the minimum to the maximum. Both the time-dependent instantaneous frequency and fluctuation amplitude vary with the time and are distributed widely, showing non-stationary and non-linear characteristics of the electrostatic signals as well as complex modulations of frequency and amplitude. On a basis of phase interactions, particle-particle and particle-wall collisions, and equipment-dominated particle random motion, the non-stationary and non-linear characteristics are caused by the interweaved modulation of particles with different velocities, the inner-wave modulation of the radial and axial particle velocity changes, and the amplitude modulation caused by particle distributions [34,47]. Moreover,

Figure 5 reveals that the energy distribution of electrostatic signals shifts from higher to lower frequencies with the solids flux, due to the enhanced formation of particle clusters, which occur intermittently with lower frequencies than the individual particles in a diluter suspension. Therefore, the Hilbert spectra of electrostatic signals allow the identification of local solids behaviours in the riser.

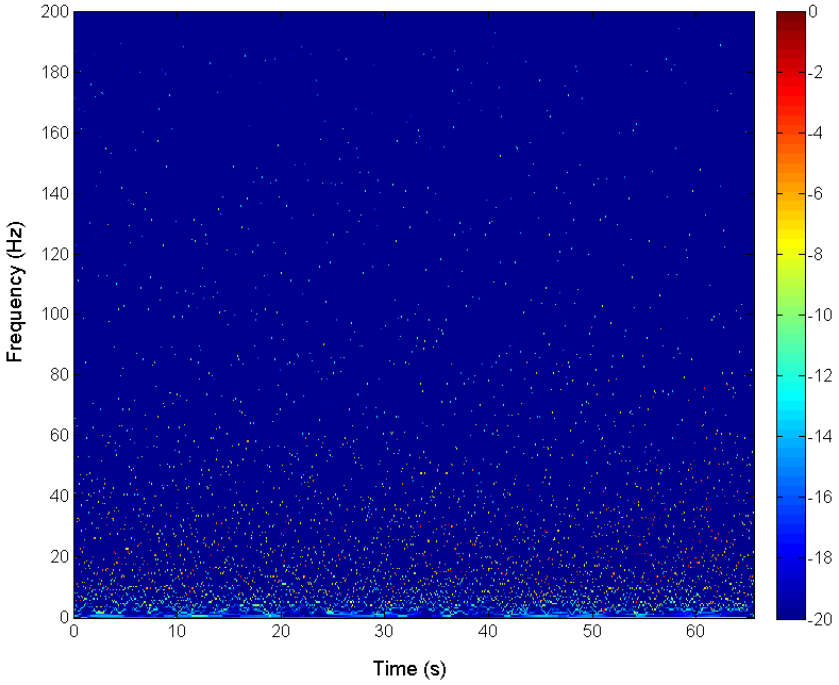

(a) G_s=4.0 kg/(m^2·s)

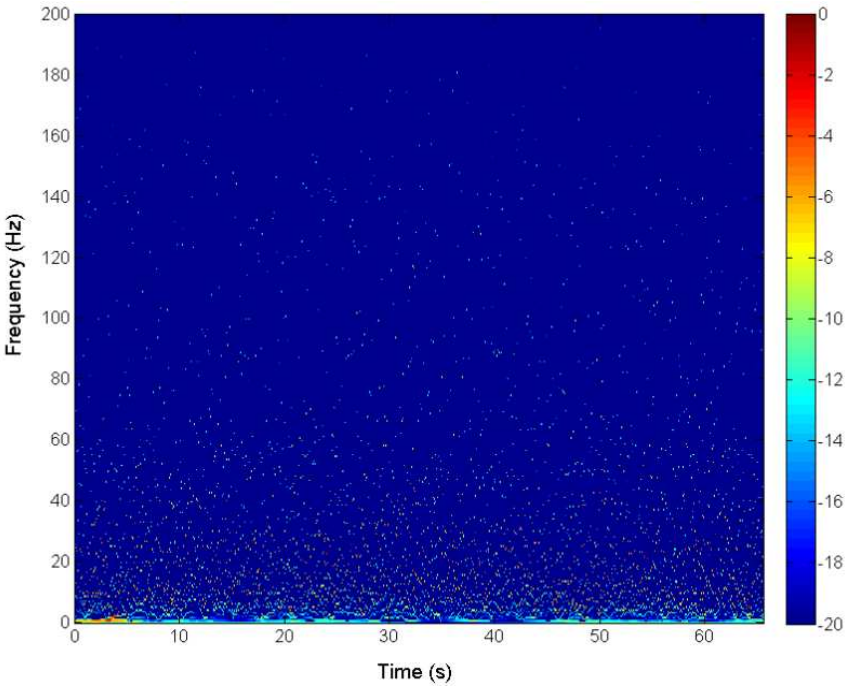

(b) G_s=8.0 kg/(m^2·s)

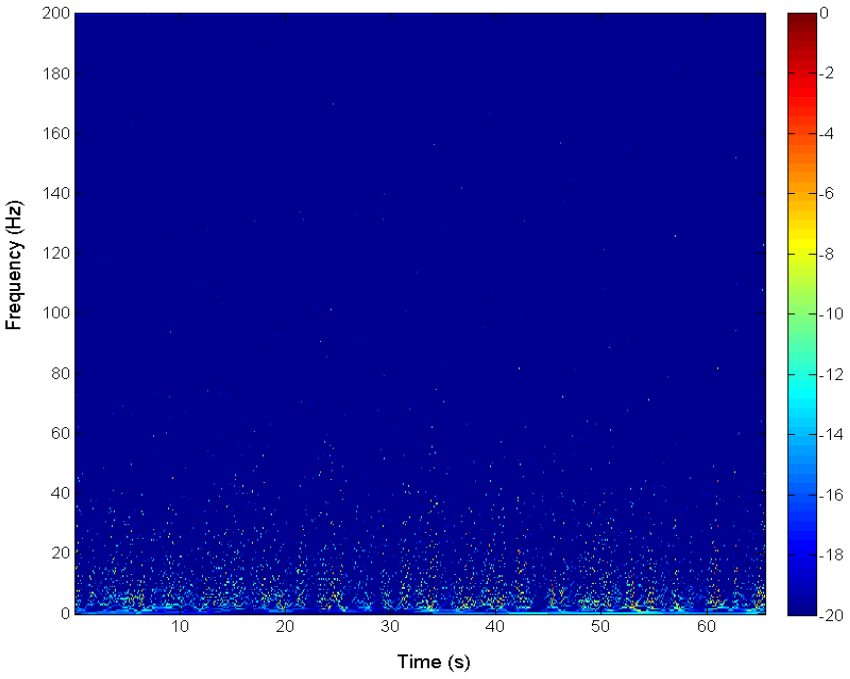

(c) G_s=35.0 kg/(m^2·s)

Figure 5. Hilbert spectra of the electrostatic signals from the left sensor array 3 under different operation conditions, h=1870 mm, U_g=4.6 m/s

Figure 6 shows the effects of solids flux on the energy distributions of the IMFs of electrostatic signals from the left sensor array 3 at h=1870 mm. At U_g=3.9 m/s and G_s=4.0 kg/(m^2·s) in Figure 6(a) the electrostatic fluctuation energy is mainly distributed at the scales of IMF3 and IMF4. With the increase of G_s to 8.0 kg/(m^2·s) the energy distribution is broadened and the scales of IMF4~IMF8 become dominant. It is known from Section 4.1 that the solids holdup increases and particles near the wall tend to form groups or clusters with the solids flux. As the motion frequency of the mesoscale clusters is lower than that of the microscale particles, the energy distribution shifts towards larger scales (lower frequencies) with the solids flux. Figures 6(b) and (c) exhibit similar variation tendencies. Especially at G_s=20.0 kg/(m^2·s) and G_s=35.0 kg/(m^2·s), a large amount of energy is occupied by IMF6~IMF10, resulting from the existence of core-annulus flow patterns and the significantly enhanced particle cluster formation. Moreover, the multiple peaks exhibited between the small and large scales at the higher G_s in Figure 6 indicate the multiple motion patterns and mesoscale characteristics of particle clusters, while the nearly single peaks at the lower G_s reflect consistent dynamic characteristics of the dilute suspensions under different conditions.

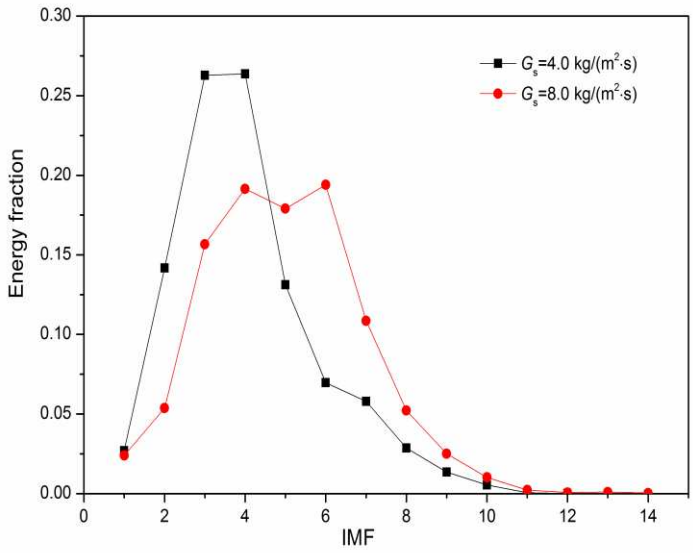

(a) U_g=3.9 m/s

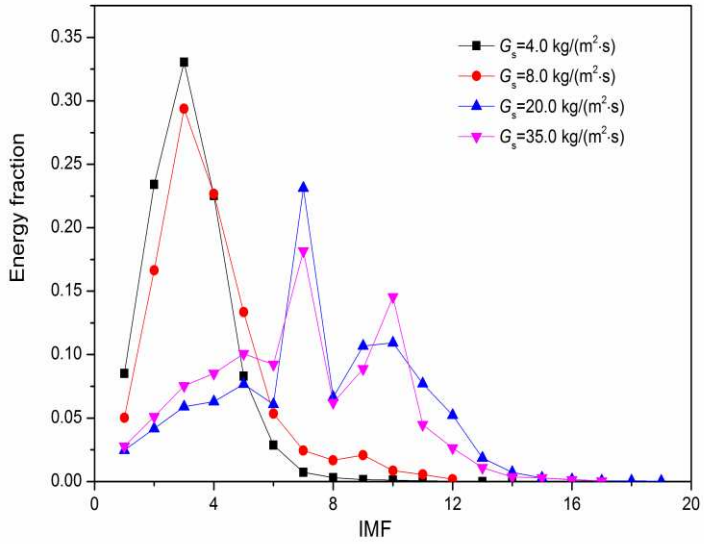

(b) U_g=4.6 m/s

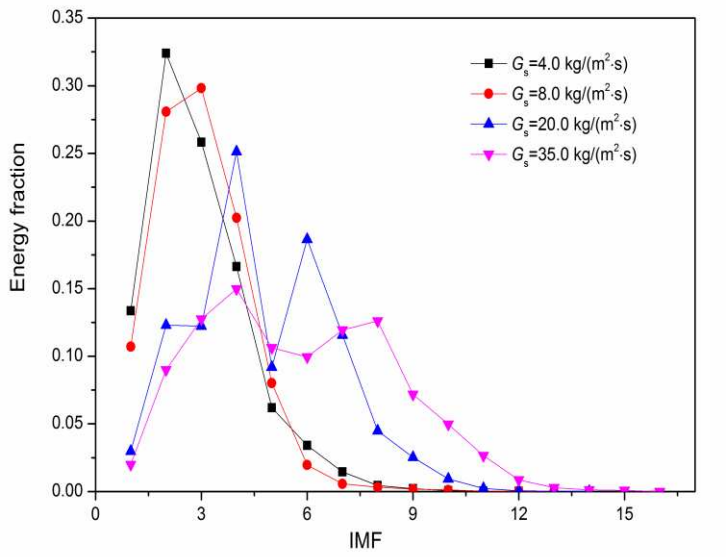

(c) U_g=5.0 m/s

Figure 6. Effects of solids flux on the energy distributions of the IMFs of electrostatic signals from the left sensor array 3, h=1870 mm

Figure 7 shows the effects of superficial gas velocity on the energy distributions of the IMFs of electrostatic signals from the left sensor array 1. The results at h=580 mm are used for analysis in order to show the flow field variations in the lower region of the riser. The energy distribution shifts towards smaller scales and is narrowed evidently with the superficial gas velocity, due to the homogenised flow field and weakened influence of particle clusters. In addition, the multiple peaks indicate the multiple motion patterns and mesoscale characteristics of particle clusters in the lower region.

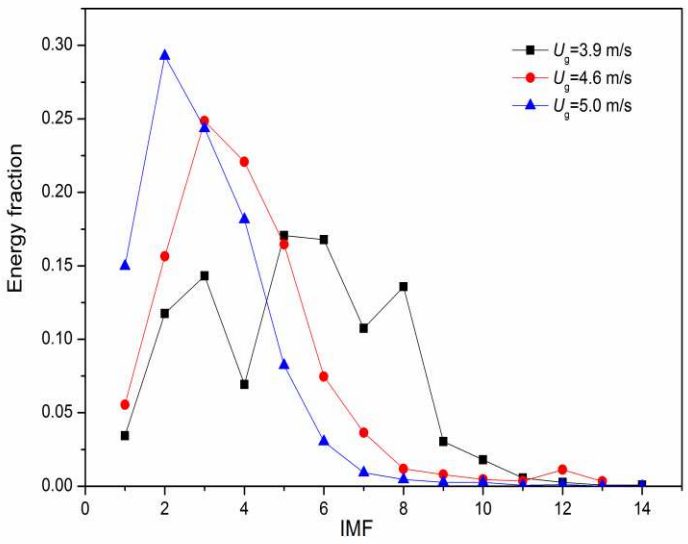

(a) G_s=8.0 kg/(m^2·s)

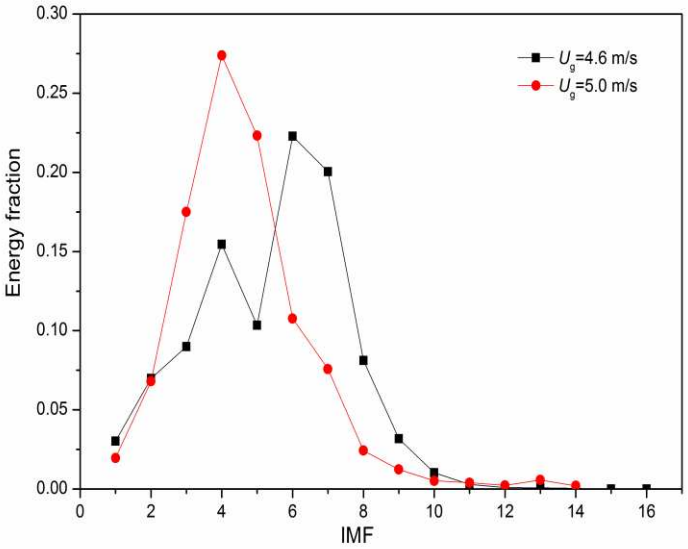

(b) G_s=20.0 kg/(m^2·s)

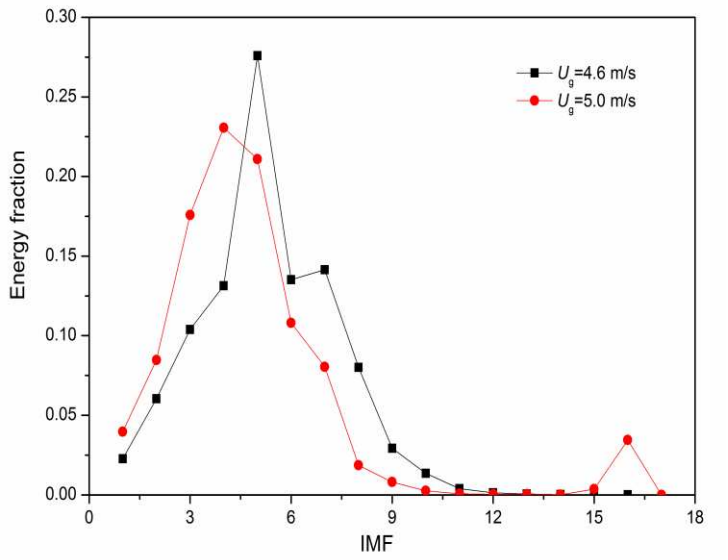

(c) G_s=35.0 kg/(m^2·s)

Figure 7. Effects of superficial gas velocity on the energy distributions of the IMFs of electrostatic signals from the left sensor array 1, h=580 mm

The effects of operation conditions on the flow homogeneity are further studied by comparing the energy distributions of the IMFs of electrostatic signals collected at different positions, as shown in Figures 8. With the increase of G_s, all the distributions are broadened and shift towards larger scales, indicating intensified formation and motion of particle clusters in the whole riser. In addition, differences in the distribution profiles are enhanced significantly at G_s=20.0 kg/(m^2·s) and G_s=35.0 kg/(m^2·s), due to the existence of core-annulus flow patterns and the non-uniform solids distributions in the riser. Specifically, the mesoscale clusters paly as intermittent energy carriers, whose variations in the dimension, solids holdup and velocity all lead to heterogeneity of the flow field.

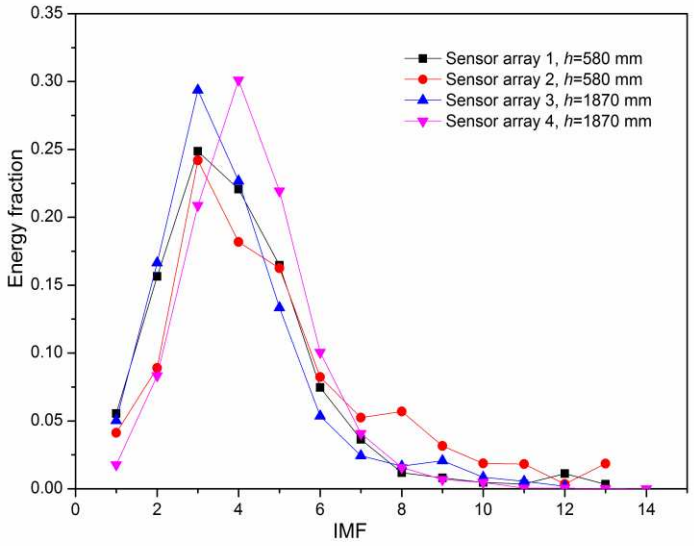

(a) G_s=8.0 kg/(m^2·s)

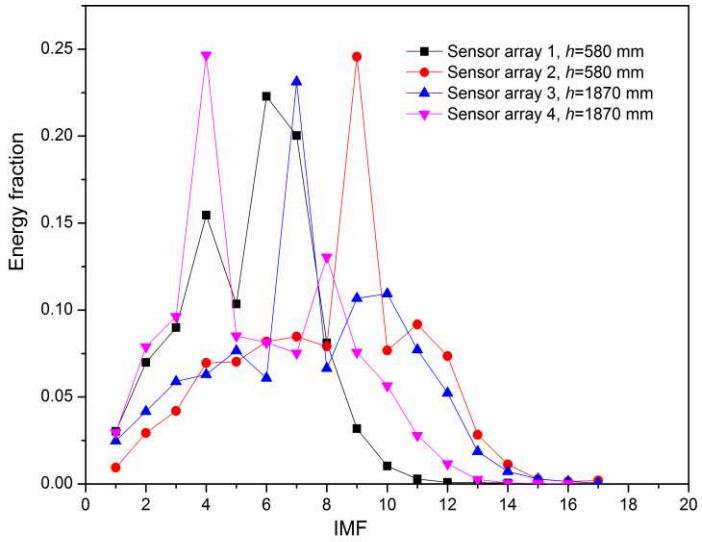

(b) G_s=20.0 kg/(m^2·s)

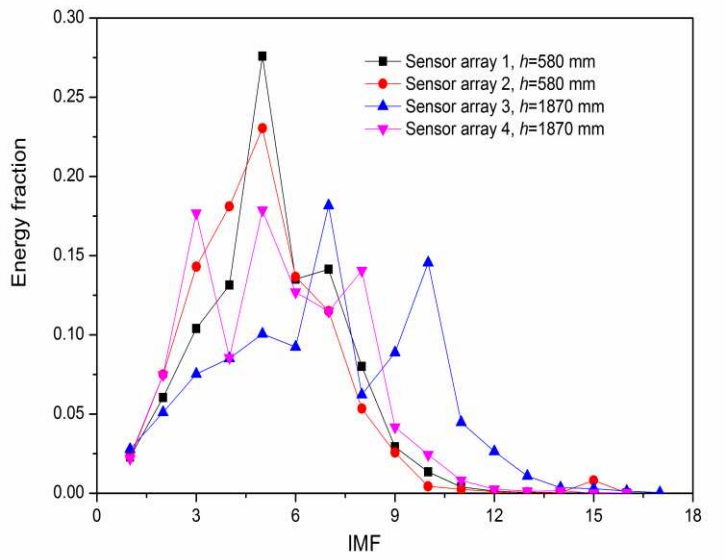

(c) G_s=35.0 kg/(m^2·s)

Figure 8. Energy distributions of the IMFs of electrostatic signals from the sensor arrays 1 to 4 at U_g=4.6 m/s

4.2.2. Vibration signal analysis

The vibration signals acquired are resampled to 400 Hz prior to HHT for the sake of comparison with the results from the electrostatic signals. Figure 9 shows the Hilbert spectra of vibration signals from the upper accelerometer at U_g=4.6 m/s, describing the local characteristics and time-frequency-energy distribution of the fluctuation signals. Both the time-dependent instantaneous frequency and fluctuation amplitude vary with the time and are distributed widely, showing non-stationary and non-linear characteristics of the vibration signals as well as complex modulations of frequency and amplitude, similar to Figure 5. Such characteristics are mainly dominated by phase interactions, particle-particle and particle-wall collisions, and structure resonance of the riser. In addition, the vibration energy distribution shifts from higher to lower

frequencies with the solids flux, due to the enhanced motion of mesoscale clusters and their strengthened intermittent impacts on the riser wall. Hence, the Hilbert spectra of vibration signals allow the identification of local solids behaviours in the riser. However, the energy variation shown in Figure 9 is less significant than that in the electrostatic Hilbert spectra (Figure 5), as the vibration signals are determined by more complex hydrodynamic and mechanical factors than the electrostatic signals, and the effects of cluster occurrences are relatively weakened.

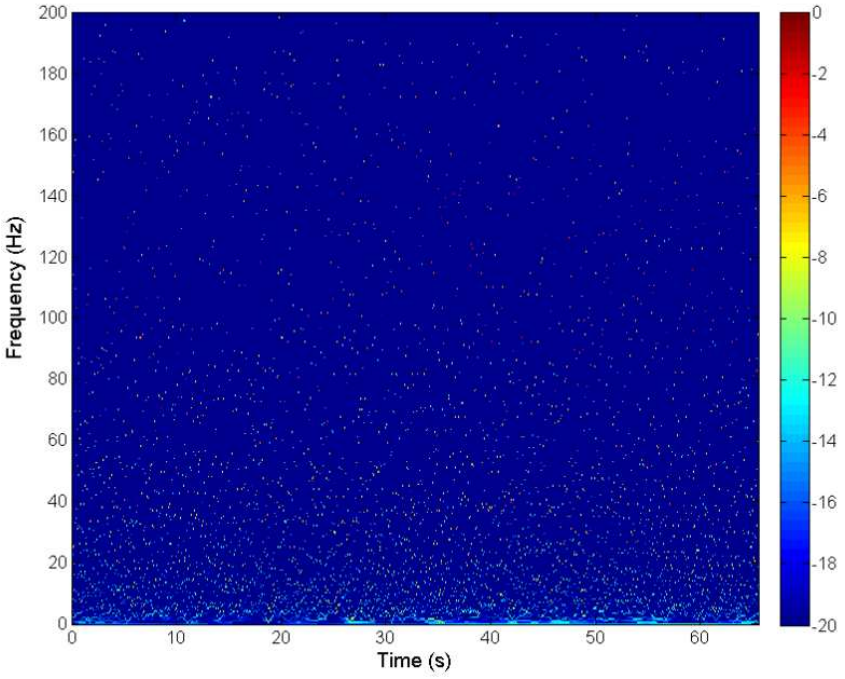

(a) G_s=4.0 kg/(m^2·s)

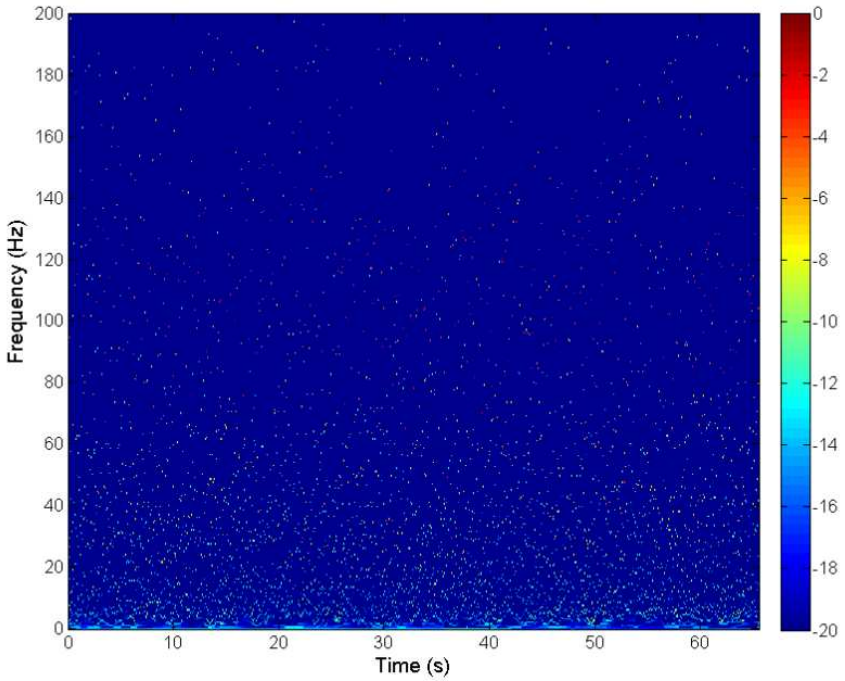

(b) G_s=8.0 kg/(m^2·s)

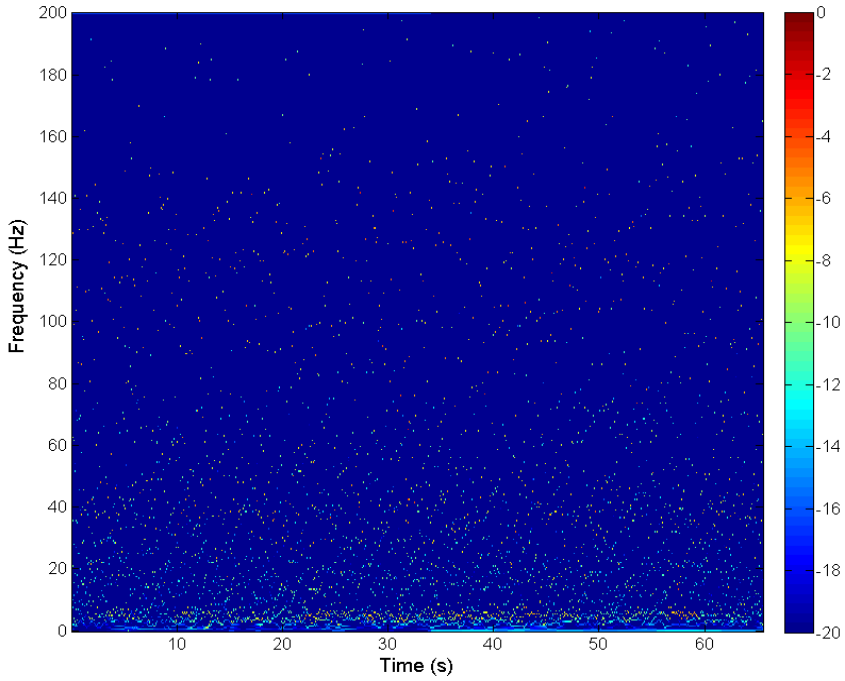

(c) G_s=35.0 kg/(m^2·s)

Figure 9. Hilbert spectra of vibration signals from the upper accelerometer under different operation conditions, h=1940 mm, U_g=4.6 m/s

The resampled vibration signals from both accelerometers are decomposed into IMFs, and the energy distributions are plotted in Figures 10 and 11. The vibration fluctuation energy is mainly distributed at small scales, indicating that the accelerometers are highly sensitive to the high-frequency particle motion and structure resonance [48]. de Martin et al. [24] also pointed out that the vibration signals sampled on a fluidised bed were highly complex and strongly affected by the background noise, secondary mechanical vibrations, and structure resonance. Therefore, the effects of mesoscale structures, typically particle clusters, on the energy distributions of the IMFs of vibration signals are less identifiable than those of the electrostatic signals. However, Figures 10(a) and 11(a) still exhibit increased energy fractions at the mesoscales of IMF5 and IMF6 due to the enhanced cluster formation and motion at G_s=20.0 kg/($m^2 \cdot s$) and G_s=35.0 kg/($m^2 \cdot s$) with h=1940 mm. This variation tendencies are basically consistent with that shown in Figure 6. No significant changes are exhibited in the IMF energy distributions obtained from the lower accelerometer at h=650 mm, as shown in Figures 10(b) and 11(b). This is because the higher suspension density at the riser bottom homogenises the influence of cluster motion to some extent, while the diluter flow condition in the top region makes the cluster behaviours more distinct [19]. A similar finding has been reported by Mondal et al. [13]. To acquire a more clear identification of cluster behaviours from the vibration signals, V-statistic analysis is applied and discussed in the next section.

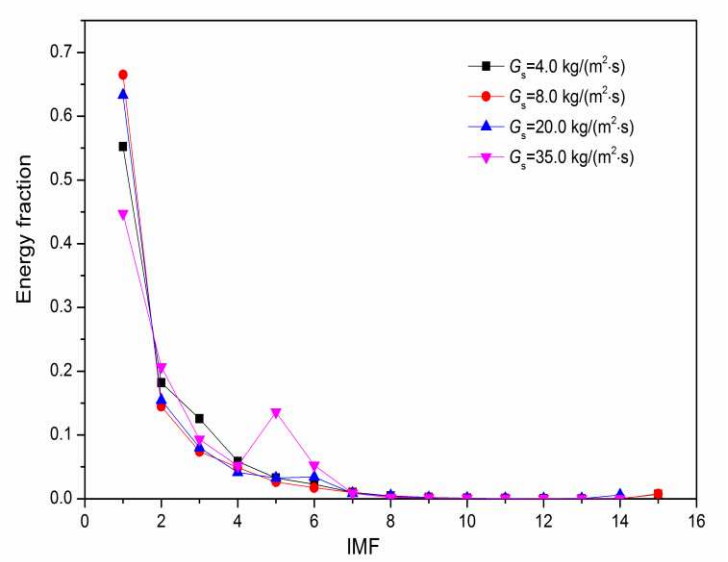

(a) Upper accelerometer, h=1940 mm

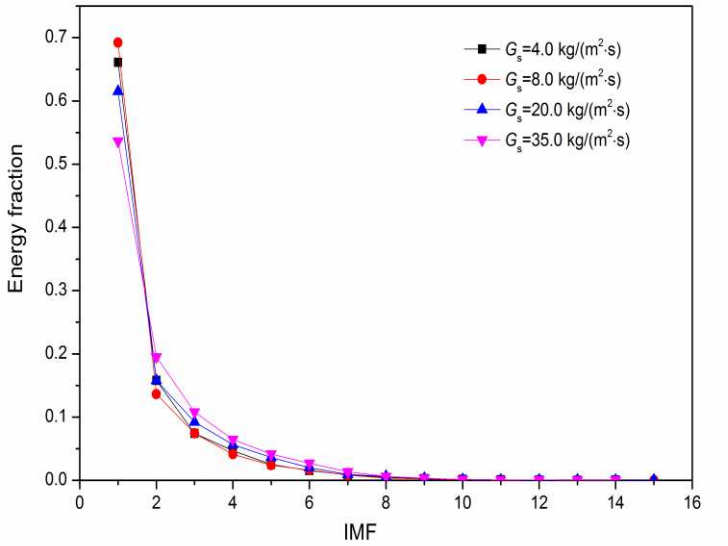

(b) Lower accelerometer, h=650 mm

Figure 10. Energy distributions of the IMFs of vibration signals from different accelerometers, U_g=4.6 m/s

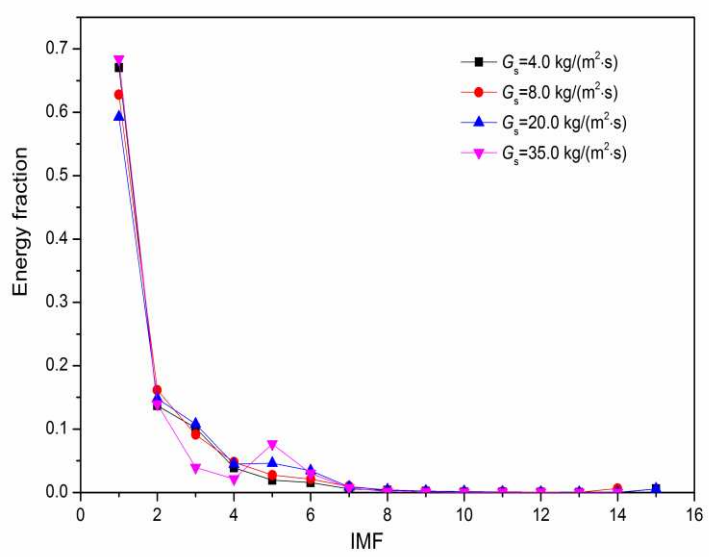

(a) Upper accelerometer, h=1940 mm

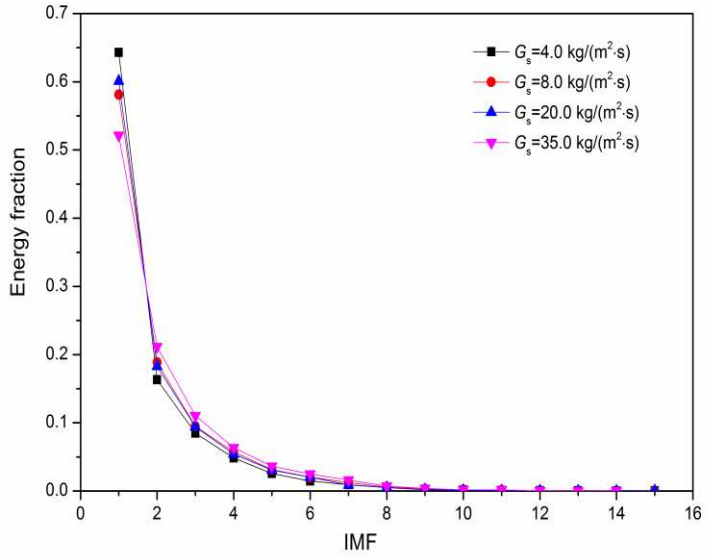

(b) Lower accelerometer, h=650 mm

Figure 11. Energy distributions of the IMFs of vibration signals from different accelerometers, U_g=5.0 m/s

4.3. V-statistic analysis and power spectral analysis

Figure 12 shows the V-statistic plots of vibration signals from the upper accelerometer under different operation conditions. Compared to the plots at G_S=4.0

kg/(m^2·s) and G_s=8.0 kg/(m^2·s), a new well-defined broad peak emerges at the lower frequencies (around lg(n)=3.5) at the higher G_s, indicating a cyclic feature of cluster motion with a main cycle time of 0.2 s and a main cycle frequency of 5.0 Hz.

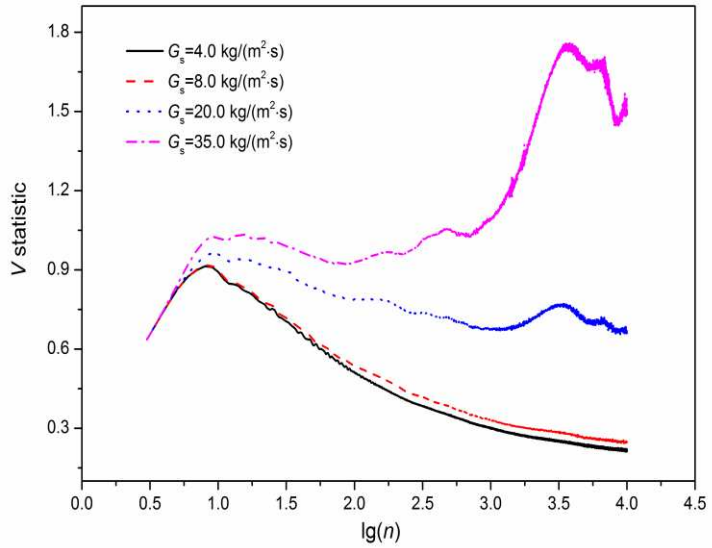

(a) U_g=4.6 m/s

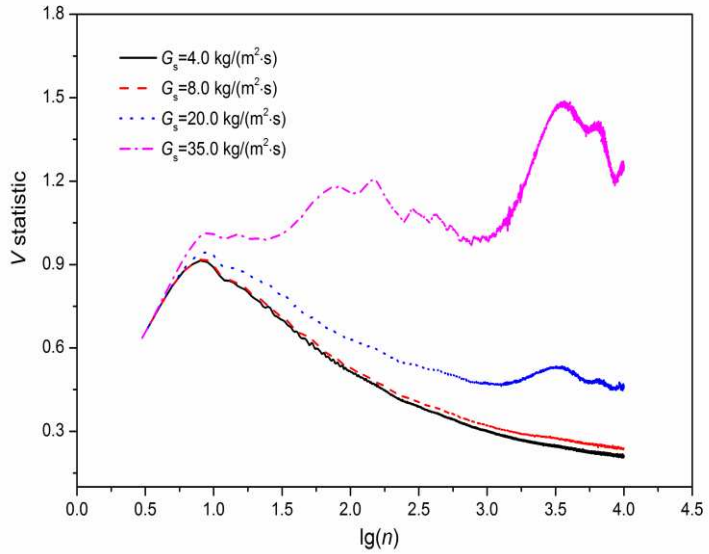

(b) U_g=5.0 m/s

Figure 12. V-statistic plots of vibration signals from the upper accelerometer under different operation conditions, h=1940 mm

According to Figures 6(b) and (c), the characteristic electrostatic signals of particle clusters are mainly reflected in the mesoscale components IMF6~IMF10. For the sake of comparison with Figure 12, the results at G_s=20.0 kg/(m^2·s) shown in Figures 6(b) and (c) are analysed as an example and the corresponding normalised power spectra are given in Figure 13. Here the 'normalisation' processing refers to

$$C_i(t) = \frac{c_i(t) - \mu}{\sigma} \tag{26}$$

where $c_i(t)$ is the ith IMF signal, μ the mean of $c_i(t)$, σ the standard deviation of $c_i(t)$, and $C_i(t)$ the normalised version of $c_i(t)$. Figure 13 shows that the weighted average frequencies of IMF7 and IMF10 at U_g=4.6 m/s are 9.1 Hz and 4.5 Hz, respectively, while that of IMF6 at U_g=5.0 m/s is 5.2 Hz. Hence, the main cycle frequency of particle clusters (5.0 Hz) indicated by the V-statistic plots basically agrees with these weighted average frequencies, indicating that consistent characteristic information about particle clusters is extracted from the electrostatic and vibration signals, and both HHT and V-statistic analysis enable the cluster behaviour characterisation in the riser.

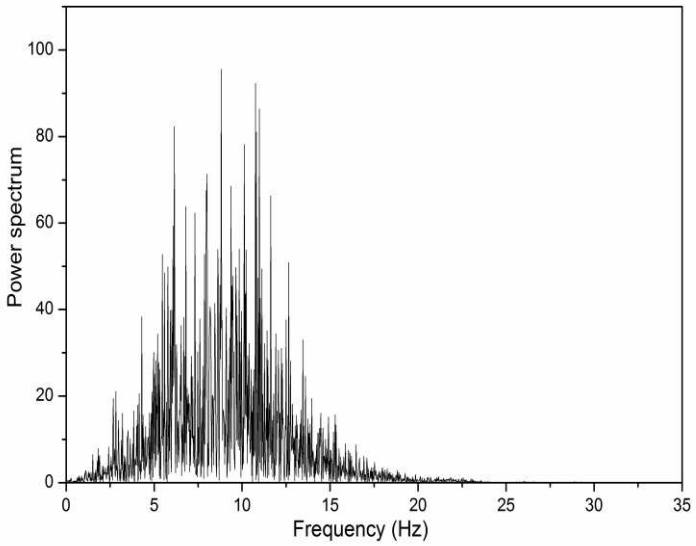

(a) U_g=4.6 m/s, IMF7

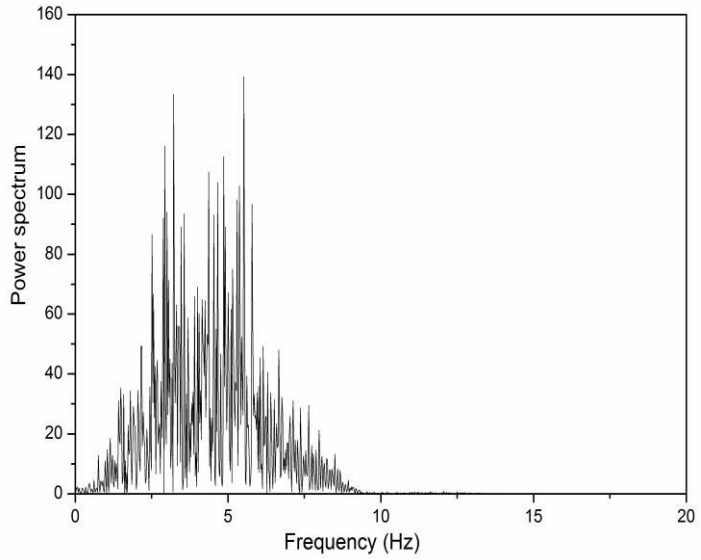

(b) U_g=4.6 m/s, IMF10

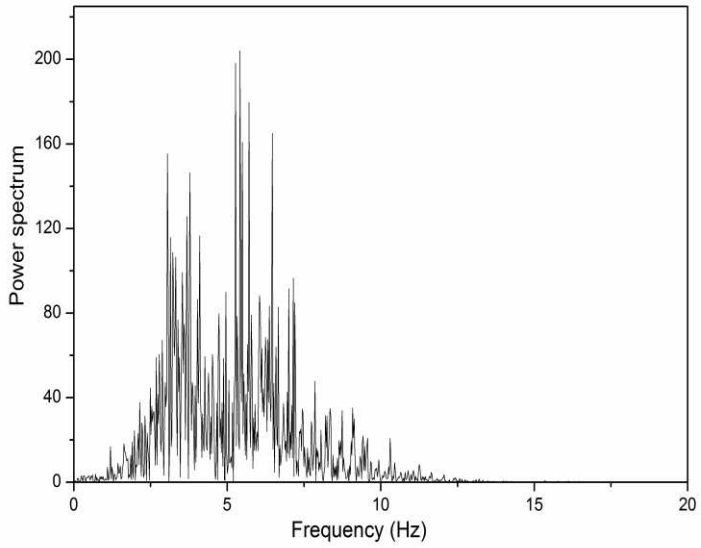

(c) U_g=5.0 m/s, IMF6

Figure 13. Normalised power spectra of the IMFs of electrostatic signals from the left sensor array 3, h=1870 mm, G_s=20.0 kg/(m^2·s)

4.4. Particle cluster identification and characterisation

4.4.1. Determination of fixed and wavelet dynamic thresholds

When particle clusters pass through an electrode, the electrostatic signal sensed exhibits significant different characteristics from that without the occurrence of particle clusters, as displayed in Figure 14. The signal segment without cluster occurrence shows random fluctuations around the mean with a low standard deviation, while that under the cluster effects results in highly intermittent voltage peaks with large amplitudes. It is known that under a saturated charged state, the amplitudes of an electrostatic signal are mainly determined by solids velocity and concentration. Recalling Figures 4(b) and (c), the solids velocity magnitudes with cluster occurrence (e.g. at G_s=20.0 kg/(m^2·s)) are smaller than or similar to those without clusters (e.g. at G_s=8.0 kg/(m^2·s)). Therefore, the high electrostatic peaks shown in Figure 14(b) are caused by the high solids holdup and particle numbers inside the clusters. This characteristic is used for cluster identification from the electrostatic signals in this study.

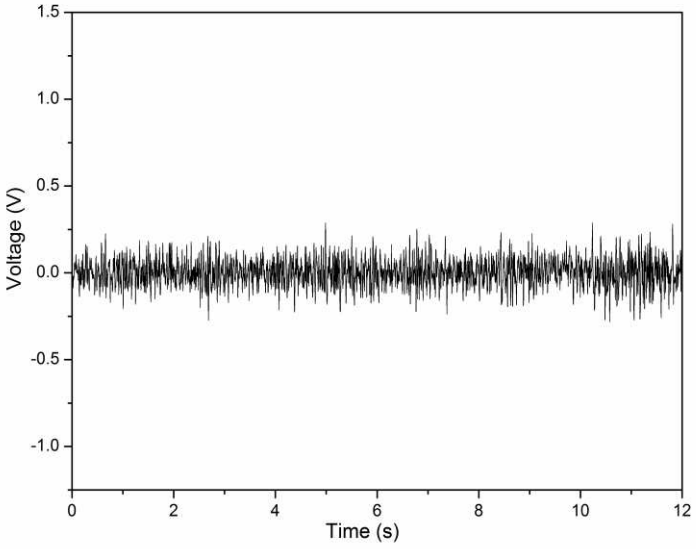

(a) G_s=8.0 kg/(m^2·s), without clusters

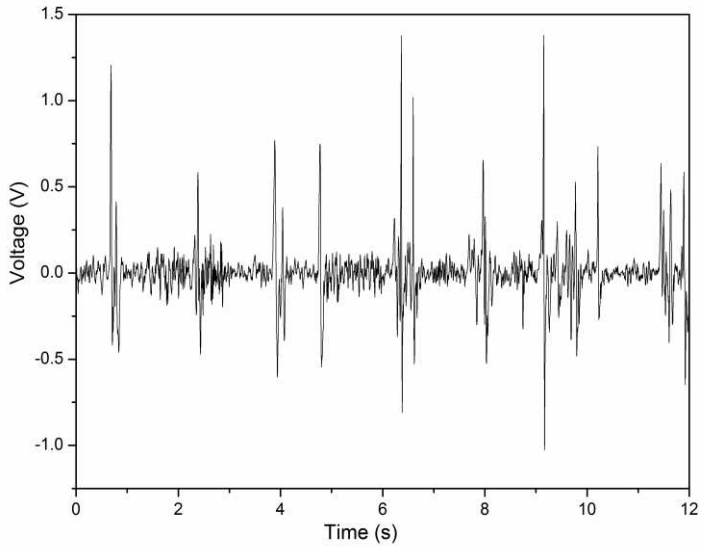

(b) G_s=20.0 kg/(m^2·s), with clusters

Figure 14. Electrostatic signals with and without cluster occurrence from the left sensor array 3, h=1870 mm, U_g=5.0 m/s

According to our preliminary analysis, the electrostatic signals under different operation conditions without cluster occurrence all fluctuate within a range of -0.3~0.3 V. Therefore, time-independent thresholds, ± 0.15 V, are first applied to the electrostatic signals under G_s=20.0 kg/(m^2·s) and G_s=35.0 kg/(m^2·s) for a rough separation between the cluster and individual-particle signals. However, such fixed thresholds may lead to dynamic information loss and inaccurate cluster characterisation. Wavelet transform is hence employed for the determination of a dynamic threshold following the fixed thresholds. In this study, signal points above 0.15 V and below -0.15 V, denoted by $x_{thr}(t)$, are decomposed into 14 scales through Daubechies3. As the approximation subsignals at different levels reflect the variations of the original signal

in different frequency bands, a specific approximation subsignal can be considered as the dynamic threshold, which allows both the cluster identification and dynamic feature retention [29]. Signal points above this dynamic threshold are then discerned as particle clusters. Although the time-independent threshold value used for a rough signal separation is dependent on the sensor and signal conditioning electronics used, the combination of the time-independent and dynamic thresholds enables an accurate extraction of cluster signals. Figure 15 shows a segment of $x_{thr}(t)$ under U_g=4.6 m/s and G_s=20.0 kg/(m^2·s) and the corresponding approximation subsignals A_4~A_7. With the decrease of the level, the subsignal amplitudes increase and more high peaks representing cluster occurrence are covered by the subsignal. While with the decrease of the level, the subsignal becomes smoother and closer to the mean of $x_{thr}(t)$. The selection of an approximation subsignal as the dynamic threshold affects directly the cluster identification and further the cluster parameter estimation. A too high or too low wavelet level may lead to deviations from the actual parameter values. In order to determine a suitable level for cluster identification, the effects of levels on cluster characteristic parameters at different positions and operation conditions are studied. The variations of cluster frequency f_{cl} are taken as an example, as shown in Figure 16. The approximation subsignal level at which the cluster frequency reaches the minimum or a stable value is chosen as a compromised threshold level, j=5 in this work. A cluster is then identified when the electrostatic signal amplitude exceeds the amplitude of A_5, and exists until the signal amplitude drops below the amplitude of A_5.

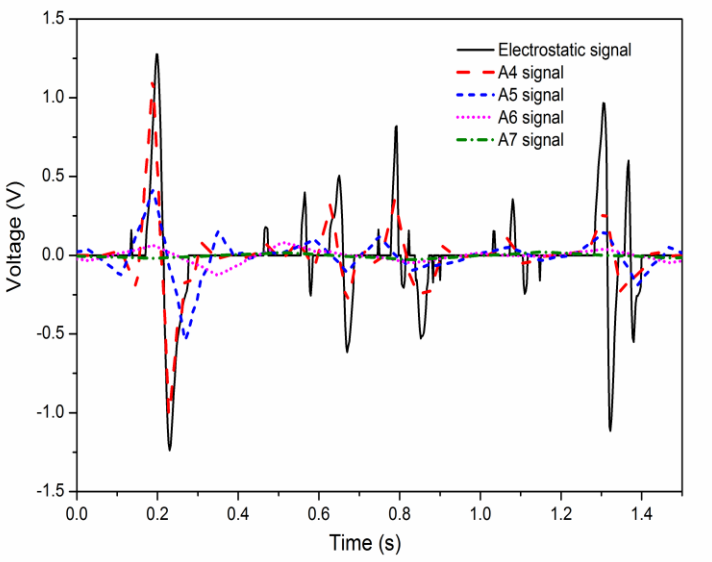

Figure 15. A segment of $x_{thr}(t)$ and the corresponding approximation subsignals A_4~A_7 from the left sensor array 3, h=1870 mm, U_g=4.6 m/s, G_s=20.0 kg/(m^2·s)

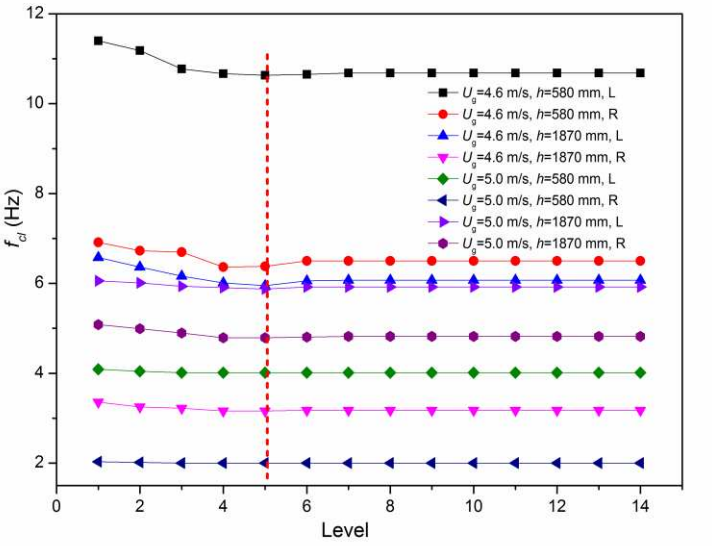

(a) G_s=20.0 kg/(m^2·s)

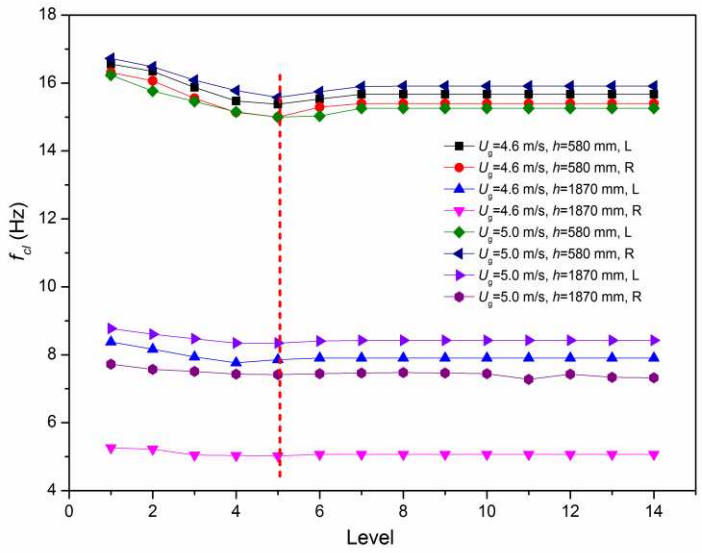

(b) G_s=35.0 kg/(m^2·s)

Figure 16. Effects of wavelet levels on cluster frequencies at different positions and operation conditions, L: from a left sensor array, R: from a right sensor array

4.4.2. Cluster parameter analysis

Figure 17~20 show the cluster characteristic parameters calculated from the electrostatic signals, based on the aforementioned cluster identification criterion, including a fixed and a wavelet dynamic thresholds. The cluster frequency, f_{cl}, shown in Figure 17 decreases basically with the height because of the higher solids holdup and particle motion intensity in the lower region than those at the top region, leading to more frequent formation and identification of particle clusters. However, the dense suspension and strong particle motion in the lower region also make f_{cl} highly sensitive to flow field changes. f_{cl} hence exhibits strong fluctuation with the height at h=560~600 mm, despite the short electrode spacing. In addition, f_{cl} increases significantly with the solids flux and decreases with the gas velocity, indicating enhanced and weakened

cluster formation and motion, respectively. This is consistent with the conclusions obtained from HHT analysis (Section 4.2). The insignificant decrease or even slight increase of f_{cl} with the gas velocity at h=1850~1870 mm is attributed to the relative low solids holdup in the riser at G_s=20.0 kg/(m^2·s), especially at the top. The differences between f_{cl} obtained from the left and right sensor arrays indicate the heterogeneous solids flow and cluster distributions under the core-annulus flow patterns. Moreover, compared with the cluster 'main cycle frequency' of 5.0 Hz at h=1870 mm (left) obtained from the vibration signal analysis (Section 4.3), the corresponding f_{cl} given in Figure 17 is 5.95 Hz, 7.86 Hz, and 5.87 Hz under the three conditions of U_g=4.6 m/s and G_s=20.0 kg/(m^2·s), U_g=4.6 m/s and G_s=35.0 kg/(m^2·s), and U_g=5.0 m/s and G_s=20.0 kg/(m^2·s), respectively, indicating good consistency of the cluster motion characteristics and verification of the cluster identification criterion used in this study.

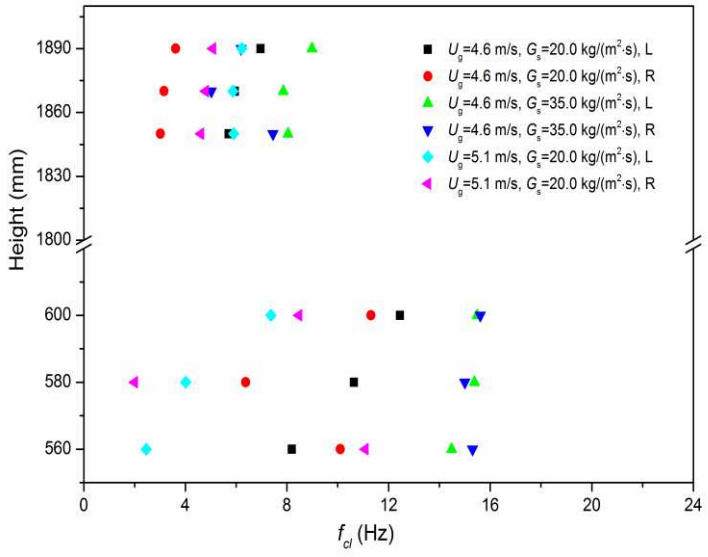

Figure 17. Cluster frequencies at different positions and operation conditions (L: from a left sensor array, R: from a right sensor array)

Figure 18 shows the cluster time fractions, F_{cl}, at different positions and operation conditions. Similar to f_{cl}, F_{cl} at the top is lower than that at the lower region, mainly due to the relatively dilute condition at the top and the less occurrence of particle clusters. F_{cl} increases with the solids flux and decreases with superficial gas velocity due to the strengthened and weakened cluster formation, respectively.

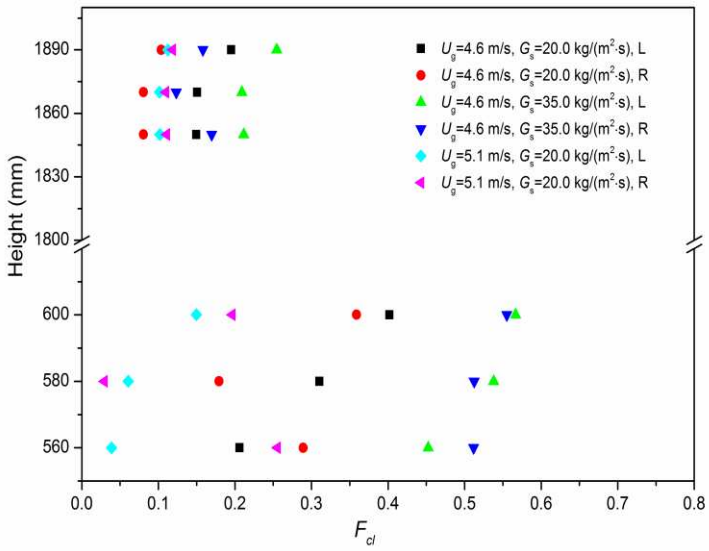

Figure 18. Cluster time fractions at different positions and operation conditions (L: from a left sensor array, R: from a right sensor array)

The average cluster duration times, τ_{cl}, at different positions and operation conditions are given in Figure 19. The variation tendency of τ_{cl} with the height is not as obvious as those for f_{cl} and F_{cl}. Nevertheless, τ_{cl} increases with the solids flux and decreases significantly with the superficial gas velocity. This is because particle clusters are prone to remain their forms at a higher solids holdup due to the shorter mean free path of particles, while tend to disintegrate into individual particles at a higher gas velocity. In addition, the cluster duration times obtained in this study are comparable

with those reported by other researchers [28,29,49], despite a wide range of operation conditions and bed geometries employed.

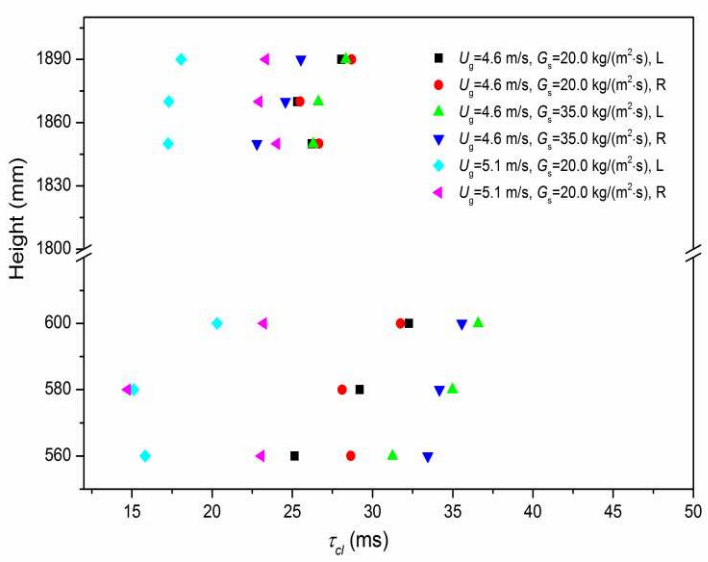

Figure 19. Average cluster duration times at different positions and operation conditions (L: from a left sensor array, R: from a right sensor array)

Figure 20 shows the average cluster vertical sizes, L_{cl}, at different positions and operation conditions. In most situations L_{cl} at the top is smaller than that in the lower region, as large clusters are more likely to be formed in the denser suspension at the bottom. Besides, L_{cl} increases with the solids flux and decreases with the superficial gas velocity due to the enhanced and weakened formation of particle clusters, respectively, except for the unusual variations at the top under U_g=4.6 m/s and G_s=20.0 kg/(m^2·s). The similar variation tendencies of L_{cl} on the left and right sides with the operation conditions indicate similar effects of operation conditions on solids flow in the radial direction. The unusual variations of L_{cl} at the top is because the estimated cluster size is dependent on both the average solids velocity and cluster duration time.

Opposite changes of the two parameters or the solids velocity varying from negative to positive lead to more complex influence on L_{cl}. In addition, the magnitudes of L_{cl} on the two sides show obvious differences, due to the non-uniform nature of gas-solid flow field and the influence of the asymmetric particle back-feeding structure.

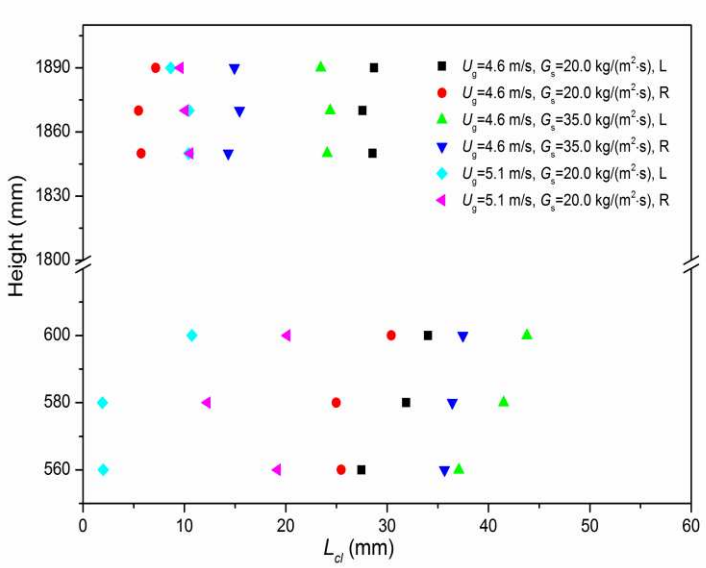

Figure 20. Average cluster vertical sizes at different positions and operation conditions (L: from a left sensor array, R: from a right sensor array)

5. Conclusions

A twelve-channel electrostatic sensing system based on arc-shaped electrodes and two accelerometers have been used on the riser of a CFB test rig. Cross correlation, HHT, V-statistic analysis, and wavelet transform have been applied to processing the electrostatic and vibration signals for the characterisation of particle cluster behaviours and their effects on the flow field. Flow patterns are indicated by the time-averaged solids velocity distributions obtained from the electrostatic signals. Non-stationary and non-linear characteristics are distinctly observed in the Hilbert spectra of the

electrostatic and vibration signals. The energy distributions of the IMFs of electrostatic signals are broadened and shift towards lower frequencies with the solids flux due to the enhanced cluster formation and motion, and are narrowed and shift towards higher frequencies with the superficial gas velocity because of the homogenised flow field. The cluster occurrence also leads to increased energy fractions at the mesoscales of the IMFs of vibration signals. Consistent characteristic information about particle clusters has been extracted from the electrostatic and vibration signals, and both HHT and V-statistic analysis enable the cluster behaviour characterisation. A cluster identification criterion for electrostatic signals has been proposed, based on which the cluster frequency, cluster time fraction, average cluster duration time, and average cluster vertical size have been quantified. Especially, the cluster frequency obtained from the identification criterion has shown a good agreement with that from the V-statistic analysis of vibration signals. Results presented in this paper have demonstrated that the electrostatic and vibration signals generated in the riser contain important dynamic information about particle clusters, and the application of appropriate signal processing methods provides an in-depth understanding of the intrinsic hydrodynamic features of the fluidisation process.

Acknowledgements

The authors would like to acknowledge the support of Newton International Fellowships (NF141121) provided by the British Academy and the Royal Society, and the support of the Fundamental Research Funds for the Central Universities (112105*172210171).

References

[1] J.W. Chew, D.M. Parker, R.A. Cocco, C.M. Hrenya, Cluster characteristics of continuous size distributions and binary mixtures of Group B particles in dilute riser flow, Chem. Eng. J. 178 (2011) 348-358.

[2] J.W. Chew, R. Hays, J.G. Findlay, T.M. Knowlton, S.B.R. Karri, R.A. Cocco, C.M. Hrenya, Cluster characteristics of Geldart Group B particles in a pilot-scale CFB riser. I. Monodisperse systems, Chem. Eng. Sci. 68 (2012) 72-81.

[3] D.N. Mondal, S. Kallio, H. Saxen, J. Hassel, Experimental study of cluster properties in a two-dimensional fluidized bed of Geldart B particles, Powder Technol. 291 (2016) 420-436.

[4] J.Y. Sun, Y. Yan, Non-intrusive measurement and hydrodynamics characterization of gas-solid fluidized beds: a review, Meas. Sci. Technol. 27 (2016) 112001.

[5] B. Zou, H.Z. Li, Y.S. Xia, X.H. Ma, Cluster structure in a circulating fluidized-bed, Powder Technol. 78 (1994) 173-178.

[6] J. Werther, Measurement techniques in fluidized beds, Powder Technol. 102 (1999) 15-36.

[7] C. Guenther, R. Breault, Wavelet analysis to characterize cluster dynamics in a circulating fluidized bed, Powder Technol. 173 (2007) 163-173.

[8] A. Kiani, R. Sotudeh-Gharebagh, N. Mostoufi, Cluster size distribution in the freeboard of a gas-solid fluidized bed, Powder Technol. 246 (2013) 1-6.

[9] C. Soong, K. Tuzla, J. Chen, Identification of particle clusters in circulating fluidized beds, Avidan, A. (Ed.), Circulating Fluidized Bed Technology IV, New York: AIChE, (1993) 809-814.

[10] A.K. Sharma, K. Tuzla, J. Matsen, J.C. Chen, Parametric effects of particle size and gas velocity on cluster characteristics in fast fluidized beds, Powder Technol. 111 (2000) 114-122.

[11] J.W. Chew, R. Hays, J.G. Findlay, T.M. Knowlton, S.B.R. Karri, R.A. Cocco, C.M. Hrenya, Cluster characteristics of Geldart group B particles in a pilot-scale CFB riser. II. Polydisperse systems, Chem. Eng. Sci. 68 (2012) 82-93.

[12] M. Horio, H. Kuroki, Three-dimensional flow visualization of dilutely dispersed solids in bubbling and circulating fluidized beds, Chem. Eng. Sci. 49 (1994) 2413-2421.

[13] D.N. Mondal, S. Kallio, H. Saxen, Length scales of solid clusters in a two-dimensional circulating fluidized bed of Geldart B particles, Powder Technol. 269 (2015) 207-218.

[14] D. Noymer, L.R. Glicksman, Cluster motion and particle-convective heat transfer at the wall of a circulating fluidized bed, Int. J. Heat Mass Transfer 41 (1998) 147-158.

[15] K.Z. Dong, Q. Zhang, Z.L. Huang, Z.W., Liao, J.D. Wang, Y.R. Yang, F. Wang, Experimental investigation of electrostatic effect on particle motions in gas-solid fluidized beds, AIChE J. 61 (2015) 3628-3638.

[16] Y. Yang, Z.L. Huang, W.B. Zhang, J.D. Wang, M. Lungu, Z.W. Liao, F. Wang, Y.R. Yang, Y. Yan, J. Yang, Effects of agglomerates on electrostatic behaviors in gas-solid fluidized beds, Powder Technol. 287 (2016) 139-151.

[17] W.B. Zhang, Y.P. Cheng, C. Wang, W.Q. Yang, C.H. Wang, Investigation on hydrodynamics of triple-bed combined circulating fluidized bed using electrostatic sensor and electrical capacitance tomography, Ind. Eng. Chem. Res. 52 (2013) 11198-11207.

[18] W.B. Zhang, Y. Yan, Y.R. Yang, J.D. Wang, Measurement of flow parameters in a bubbling fluidized bed using electrostatic sensor arrays, International Instrumentation and Measurement

Technology Conference, Pisa, Italy, 2015.

[19] J.Y. Sun, Y. Yan, Characterization of flow intermittency and coherent structures in a gas−solid circulating fluidized bed through electrostatic sensing, Ind. Eng. Chem. Res. 55 (2016) 12133-12148.

[20] G. Book, K. Albion, L. Briens, C. Briens, F. Berruti, On-line detection of bed fluidity in gas-solid fluidized beds with liquid injection by passive acoustic and vibrometric methods, Powder Technol. 205 (2011) 126-136.

[21] G.D. Cody, R.J. Bellows, D.J. Goldfarb, H.A. Wolf, G.V. Storch, A novel non-intrusive probe of particle motion and gas generation in the feed injection zone of the feed riser of a fluidized bed catalytic cracking unit, Powder Technol. 110 (2000) 128-142.

[22] M. Abbasi, R. Sotudeh-Gharebagh, N. Mostoufi, M.J. Mahjoob, Non-intrusive monitoring of bubbles in a gas-solid fluidized bed using vibration signature analysis, Powder Technol. 196 (2009) 278-285.

[23] H. Azizpour, R. Sotudeh-Gharebagh, R. Zarghami, M. Abbasi, N. Mostoufi, M.J. Mahjoob, Characterization of gas-solid fluidized bed hydrodynamics by vibration signature analysis, Int. J. Multiphase Flow 37 (2011) 788-793.

[24] L. de Martin, J.V. Briongos, J.M. Aragon, M.C. Palancar, Can low frequency accelerometry replace pressure measurements for monitoring gas-solid fluidized beds? Chem. Eng. Sci. 65 (2010) 4055-4064.

[25] L. de Martin, J.V. Briongos, N. Garcia-Hernando, J.M. Aragon, Detecting regime transitions in gas-solid fluidized beds from low frequency accelerometry signals, Powder Technol. 207 (2011) 104-112.

[26] N. Yang, W. Wang, J.H. Li, Modeling of meso-scale structures in particle-fluid systems: the EMMS/CFD approach, China Particuology 3 (2005) 78-79.

[27] J. Zhang, P. Jiang, L. Fan, Flow characteristics of coal ash in a circulating fluidized bed, Ind. Eng. Chem. Res. 37 (1998) 1499-1509.

[28] S. Manyele, J. Pärssinen, J. Zhu, Characterizing particle aggregates in a high-density and high-flux CFB riser, Chem. Eng. J. 88 (2002) 151-161.

[29] T. Yang, L. Leu, Multiresolution analysis on identification and dynamics of clusters in a circulating fluidized bed, AIChE J. 55 (2009) 612-629.

[30] J.V. Briongos, J.M. Aragon, M.C. Palancar, Phase space structure and multi-resolution analysis of gas-solid fluidized bed hydrodynamics: Part I - The EMD approach, Chem. Eng. Sci. 61 (2006) 6963-6980.

[31] G.Z. Qiu, J.M. Ye, H.G. Wang, Investigation of gas-solids flow characteristics in a circulating fluidized bed with annular combustion chamber by pressure measurements and CPFD simulation, Chem. Eng. Sci. 134 (2015) 433-447.

[32] C.H. Wang, Z.P. Zhong, R. Li, Flow regime recognition in the spouted bed based on Hilbert-Huang transformation, Korean J. Chem. Eng. 28 (2011) 308-313.

[33] W.L. Li, W.Q. Zhong, B.S. Jin, R. Xiao, T.T. He, Flow regime identification in a three-phase bubble column based on statistical, Hurst, Hilbert-Huang transform and Shannon entropy analysis, Chem. Eng. Sci. 102 (2013) 474-485.

[34] C.L. Xu, C. Liang, B. Zhou, S.M. Wang, HHT analysis of electrostatic fluctuation signals in dense-phase pneumatic conveying of pulverized coal at high pressure, Chem. Eng. Sci. 65 (2010) 1334-1344.

[35] N.E. Huang, Z. Shen, S.R. Long, M.L.C. Wu, H.H. Shih, Q.N. Zheng, N.C. Yen, C.C. Tung, H.H. Liu, The empirical mode decomposition and the Hilbert spectrum for nonlinear and non-stationary time series analysis, Proc. R. Soc. A 454 (1998) 903-995.

[36] H.E. Hurst, Long-term storage capacity of reservoirs, Trans. Am. Soc. Civ. Eng. 116 (1951) 770-808.

[37] D. Bai, A.S. Issangya, J.R. Grace, Characteristics of gas-fluidized beds in different flow regimes, Ind. Eng. Chem. Res. 38 (1999) 803-811.

[38] N. Ellis, L.A. Briens, J.R. Grace, H.T. Bi, C.J. Lim, Characterization of dynamic behaviour in gas-solid turbulent fluidized bed using chaos and wavelet analyses, Chem. Eng. J. 96 (2003) 105-116.

[39] C.J. Ren, X.J. Jiang, J.D. Wang, Y.R. Yang, X.H. Zhang, Determination of critical speed for complete solid suspension using acoustic emission method based on multiscale analysis in stirred tank, Ind. Eng. Chem. Res. 47 (2008) 5323-5327.

[40] A. Mittal, S.S. Mallick, P.W. Wypych, An investigation into pressure fluctuations for fluidized dense-phase pneumatic transport of fine powders, Powder Technol. 277 (2015) 163-170.

[41] H. Azizpour, R. Sotudeh-Gharebagh, R. Zarghami, N. Mostoufi, Vibration time series analysis of bubbling and turbulent fluidization, Particuology 10 (2012) 292-297.

[42] E.E. Peters, Fractal Market Analysis: Applying Chaos Theory to Investment and Economics, Wiley, New York, 1994.

[43] L.A. Briens, C.L. Briens, Cycle detection and characterization in chemical engineering, AIChE J. 48 (2002) 970-980.

[44] Y.F. Zhou, C.J. Ren, J.D. Wang, Y.R. Yang, Characterization on hydrodynamic behavior in liquid-containing gas-solid fluidized bed beactor, AIChE J. 59 (2013) 1056-1065.

[45] S.G. Mallat, A Wavelet Tour of Signal Processing, Academic Press, San Diego, 1998.

[46] Y. Jin, J.X. Zhu, Z.W. Wang, Z.Q. Yu, Fluidization Engineering Principles, Tsinghua University Press, Beijing, 2001.

[47] P. Lu, D. Han, R.X. Jiang, X.P. Chen, C.S. Zhao, G.C. Zhang, Experimental study on flow patterns of high-pressure gas-solid flow and Hilbert-Huang transform based analysis, Exp. Therm Fluid Sci. 51 (2013) 174-182.

[48] J.V. Briongos, C. Sobrino, J. Gomez-Hernandez, D. Santana, Characterization of flow-induced vibrations in gas-solid fluidized beds: Elements of the theory, Chem. Eng. Sci. 93 (2013) 181-196.

[49] J. van der Schaaf, J.C. Schouten, F. Johnsson, C.M. van den Bleek, Non-intrusive determination of bubble and slug length scales in fluidized beds by decomposition of the power spectral density of pressure time series, Int. J. Multiphase Flow 28 (2002) 865-880.

Figure captions

Figure 1. Layout of the gas-solid CFB test rig

Figure 2. Top view of the electrostatic sensor arrays

Figure 3. Variations of solids velocity with the time from the left sensor array 3, U_g=5.0 m/s, G_s=20.0 kg/($m^2 \cdot s$)

Figure 4. Axial distributions of the time-averaged solids velocity from the left sensor arrays 1 and 3 under different operation conditions (a) U_g=3.9 m/s, (b) U_g=4.6 m/s, (c) U_g=5.0 m/s

Figure 5. Hilbert spectra of the electrostatic signals from the left sensor array 3 under different operation conditions, h=1870 mm, U_g=4.6 m/s (a) G_s=4.0 kg/($m^2 \cdot s$), (b) G_s=8.0 kg/($m^2 \cdot s$), (c) G_s=35.0 kg/($m^2 \cdot s$)

Figure 6. Effects of solids flux on the energy distributions of the IMFs of electrostatic signals from the left sensor array 3, h=1870 mm (a) U_g=3.9 m/s, (b) U_g=4.6 m/s, (c) U_g=5.0 m/s

Figure 7. Effects of superficial gas velocity on the energy distributions of the IMFs of electrostatic signals from the left sensor array 1, h=580 mm (a) G_s=8.0 kg/(m^2·s), (b) G_s=20.0 kg/(m^2·s), (c) G_s=35.0 kg/(m^2·s)

Figure 8. Energy distributions of the IMFs of electrostatic signals from the sensor arrays 1 to 4 at U_g=4.6 m/s (a) G_s=8.0 kg/(m^2·s), (b) G_s=20.0 kg/(m^2·s), (c) G_s=35.0 kg/(m^2·s)

Figure 9. Hilbert spectra of vibration signals from the upper accelerometer under different operation conditions, h=1940 mm, U_g=4.6 m/s (a) G_s=4.0 kg/(m^2·s), (b) G_s=8.0 kg/(m^2·s), (c) G_s=35.0 kg/(m^2·s)

Figure 10. Energy distributions of the IMFs of vibration signals from different accelerometers, U_g=4.6 m/s (a) Upper accelerometer, h=1940 mm, (b) Lower accelerometer, h=650 mm

Figure 11. Energy distributions of the IMFs of vibration signals from different accelerometers, U_g=5.0 m/s (a) Upper accelerometer, h=1940 mm, (b) Lower accelerometer, h=650 mm

Figure 12. V-statistic plots of vibration signals from the upper accelerometer under different operation conditions, h=1940 mm (a) U_g=4.6 m/s, (b) U_g=5.0 m/s

Figure 13. Normalised power spectra of the IMFs of electrostatic signals from the left sensor array 3, h=1870 mm, G_s=20.0 kg/(m^2·s) (a) U_g=4.6 m/s, IMF7, (b) U_g=4.6 m/s, IMF10, (c) U_g=5.0 m/s, IMF6

Figure 14. Electrostatic signals with and without cluster occurrence from the left sensor array 3, h=1870 mm, U_g=5.0 m/s (a) G_s=8.0 kg/(m^2·s), without clusters, (b) G_s=20.0 kg/(m^2·s), with clusters

Figure 15. A segment of $x_{thr}(t)$ and the corresponding approximation subsignals A_4~A_7 from the left sensor array 3, h=1870 mm, U_g=4.6 m/s, G_s=20.0 kg/(m^2·s)

Figure 16. Effects of wavelet levels on cluster frequencies at different positions and operation conditions, L: from a left sensor array, R: from a right sensor array (a) G_s=20.0 kg/(m^2·s), (b) G_s=35.0 kg/(m^2·s)

Figure 17. Cluster frequencies at different positions and operation conditions (L: from a left sensor array, R: from a right sensor array)

Figure 18. Cluster time fractions at different positions and operation conditions (L: from a left sensor array, R: from a right sensor array)

Figure 19. Average cluster duration times at different positions and operation conditions (L: from a left sensor array, R: from a right sensor array)

Figure 20. Average cluster vertical sizes at different positions and operation conditions (L: from a left sensor array, R: from a right sensor array)